Material-process interactions in particle bed 3D printing and the underlying physics

Dirk Lowke, Inka Mai, Emmanuel Keita, Daniel Weger, Christoph Gehlen, Friedrich Herding, Wenqiang Zuo, Nicolas Roussel, Arnaud Perrot

Material-process interactions in particle bed 3D printing and the underlying physics

Dirk Lowke [a], Inka Mai [a], Emmanuel Keita [b], Arnaud Perrot [c], Daniel Weger [d], Christoph Gehlen [d], Friedrich Herding [a], Wenqiang Zuo [b], Nicolas Roussel [b]

[a] Technische Universität Braunschweig, Institute of Building Materials, Concrete Construction and Fire Safety, Braunschweig, Germany
[b] Gustave Eiffel University, Navier Laboratory, Paris, France
[c] Université de Bretagne Sud, FRE CNRS 3744, IRDL, Lorient, France
[d] Technical University Munich, Centre for Building Materials / Ingenieurbüro Schießl Gehlen Sodeikat, Munich, Germany

Keywords: 3D Printing; Additive Manufacturing; Selective binding; Particle bed binding; Selective cement activation; Selective paste intrusion

Abstract

This paper focuses on material-process interactions in particle bed binding. After a classification of particle bed binding techniques currently available for cement-based materials, the most important material-process interactions and their underlying physics are discussed in detail for the selective cement activation (SCA) and the selective paste intrusion technique (SPI). Here, we consider the sub-processes layer application, layer compaction, fluid application, fluid penetration and after printing treatment. We show that, by varying the material and process parameters in these sub-processes, the printing process and the resulting material properties of the printed component, such as compressive strength, durability and dimensional accuracy, can be specifically controlled. Furthermore, we illustrate how these sub-processes can be both understood and described on the basis of the underlying mechanisms and physically based material models.

1 Introduction

Additive manufacturing promises the concrete industry unprecedented opportunities in terms of digitalisation and resource efficiency [1]–[10]. With the use of additive manufacturing, planning and construction methods can be fundamentally rethought. Planners will no longer be constrained by the use of system formwork but will be able to use the material only where it is structurally or functionally required, see Figure 1. This eliminates the wasteful use of materials dictated by the economic constraints of traditional construction methods. The introduction of additive manufacturing in concrete construction revises the old paradigm that material-efficient construction is uneconomical due to labour-intensive manual work. The freedom of form comes almost for free, and intelligent computer-aided design can thus potentially save valuable resources or, more generally, reduce environmental impacts [1], [8]. Furthermore, as a digital manufacturing technology, additive manufacturing offers the possibility of being linked to the digital planning environment of building information modelling (BIM), [11].

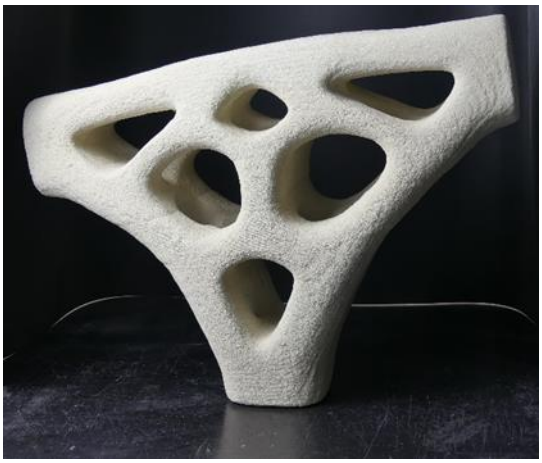

Figure 1: Topology optimised node 3D printed with Selective Cement Activation (Manufacturing: Herding, Mai, Lowke, iBMB, TU Braunschweig, Design: Kloft, ITE, TU Braunschweig)

In order to fully realise these potentials, however, a fundamental understanding of these novel additive manufacturing processes is required. Much more than with conventional technologies in concrete construction, materials and processes cannot be considered separately. Instead, it is necessary to fully account for all interactions between the process and the material. This statement applies also to the additive manufacturing process of particle bed binding [12], [13], otherwise known as particle bed 3D printing.

The essential characteristic of particle bed binding processes is the application of a particle layer in a first process step and the subsequent selective binding of the particle layer by the local application of a fluid [14], [15]. In the context of particle bed 3D printing with cement-based materials, a classification can be made between four process variants so far, see Figure 2: (a) Selective binder activation or more specific selective cement activation, (b) Selective paste intrusion, (c) Coarse aggregate binding and (d) Binder jetting.

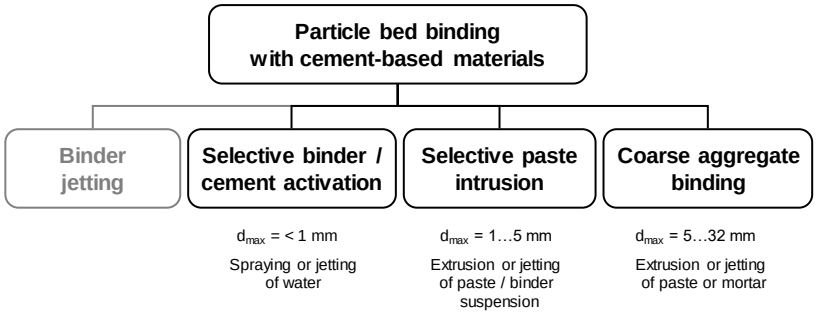

Figure 2: Extended classification of particle bed binding processes with cement-based materials from Lowke et al. [14].

In selective cement activation (SCA), the particle bed consists of a mixture of very fine aggregates (typically sand < 1 mm) and cement, which is selectively bound by local spraying or jetting of water [14]–[23],[24]. In selective paste intrusion (SPI), the particle bed consists of sand (1...5 mm) and is selectively bound by the local intrusion of a very fluid cement paste [14], [25]–[30]. The coarse aggregate binding process (CAB) is a recent development in particle bed binding. In this process variant, a coarse aggregate (typically 5...32 mm) is used for the particle bed. The coarse particle bed is then selectively bound, either by spraying mortar, as in Large Particle 3D Concrete Printing [31], or by extruding a paste, as in Aggregate-bed 3D concrete printing [32]. In contrast to SPI, the pastes or mortars are usually less fluid. It thus partially remains on the particle bed surface. When the next layer of particles is applied, it is pressed into the residual portion of the paste or mortar on the surface, which allows for a good interlayer bond

to be achieved. A major advantage of CAB is the use of coarse aggregates, which require significantly less cement per volume of concrete printed. It therefore significantly reduces the carbon footprint of the material [31]. Finally, binder jetting is a process, in which a liquid binder, typically a resin, is jetted onto a particle bed of sand and hardener. Although this process does not directly produce a concrete component, it can be used to produce free-formed formwork for concrete components [2], [33]. The layer height in particle bed 3D printing processes is typically equal to or larger than the maximum particle diameter. In the case of SCA, however, a maximum particle size larger than the layer thickness has already been used successfully with very low layer thicknesses of 0.1 mm [15].

In principle, a variety of application scenarios are feasible with particle bed 3D printing. However, a particular strength of particle bed 3D printing is its ability to produce components with an exceptionally high degree of geometrical freedom and detail. Therefore, free-formed, topology-optimised components, particularly slim components or very detailed components are particularly suitable for the fabrication with these processes. With the increasing availability of large-scale particle bed 3D printers, the first large-scale components have already been produced, e.g. bridges [13], [14], [24], slabs [33], ceilings [14], [33], [34] or façade elements [35].

In addition to the preparation of the particle mixture and the liquid phase prior to the actual printing process, the following sub-processes can be distinguished in particle bed binding processes, see Figure 3: (a) layer application, (b) layer compaction as appropriate (c) fluid application, (d) fluid penetration, (e) removal of the unbound particle bed and (f) after printing treatment.

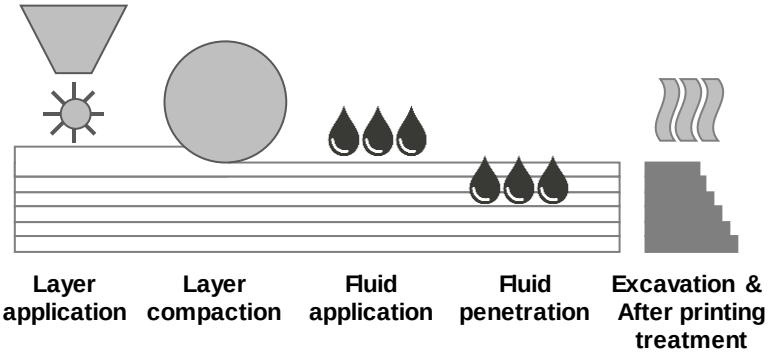

Figure 3: Sub-processes in particle bed binding

The aforementioned particular relevance of taking into account the process-material interactions in particle bed binding results from two circumstances. (I) the particle layer created in the first process step, must be completely penetrated by the fluid phase in order to guarantee high mechanical and good durability-related properties, and (II) the fluid must not move beyond the layer boundary in order to guarantee a high dimensional accuracy. With regard to high strength, a high packing density of the particles, i.e. low porosity, must also be achieved, which however can in turn negatively affect the fluid penetration. The properties of the printed material are thus affected by multiple and partly opposing interactions. In addition to the material properties of the particles and the fluid phase, there are almost all process parameters in the individual process steps that can affect the penetration of the particle bed with the fluid phase as well as the particle bed compaction.

This paper focuses on the particle bed binding techniques of Selective Cement Activation and Selective Paste Intrusion. The parameters that are decisive in the individual sub-processes of these techniques will be discussed in

detail with regard to their effect on the material properties of the printed component along with the underlying physical mechanisms.

2 Selective Cement Activation

2.1 Layer application and compaction

Layer application and compaction are the most relevant process steps in Selective Cement Activation when it comes to the packing density of the particle bed. The packing density in the particle bed is highly relevant for the mechanical performance of printed objects since it affects the coordination number, i.e. the total number of particle contacts of a single particle, as well as the liquid intrusion into the powder bed. Moreover, information about the particle bed packing are crucial for the adjustment of a defined water-cement-ratio. This can be achieved either by varying the flow rate of the liquid q (ml/min) or the travel speed of the nozzle v_n (m/s).

By varying the process conditions during layer application, the packing density of the particle bed is affected. For the presented study, various compaction levels are investigated in terms of their effect on mechanical performance. In our process using a particle bed printer of Progress (Italy), we control the level of compaction by varying the compaction height h_{comp}, i.e. the difference of the layer height before and after compacting the particle bed by a forward rotating roller with a diameter of 100 mm, see Figure 4. For example h_{comp} = 0.3 mm means that the particle bed is compacted from a height of 1.3 mm after spreading and smoothing the particles to the final layer height of 1.0 mm.

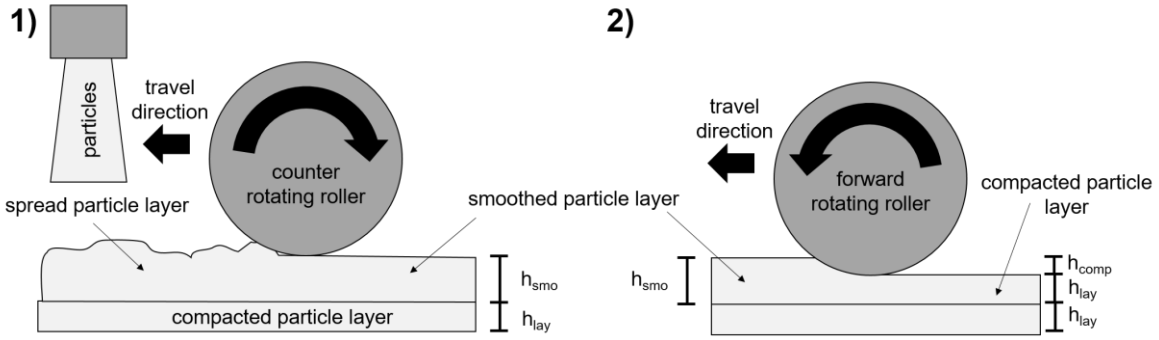

Figure 4: Schematic illustration of particle spreading and smoothing (1) and compaction (2)

Since the particle bed packing differs based on the compaction process [36] the packing density has to be measured directly in the printing process. Following [37], a hollow cylinder with a base was printed, which contained non-activated, but compacted particles, see Figure 5. In the next step, the non-activated material inside the printed cylinder was carefully removed and weighted. Furthermore, in order to take geometric imperfections of the printed cylinder into account, the filling volume was determined experimentally. Therefore, two methods were used and compared. For the first method, the hollow cylinders are scanned with a µCT and the inner volume of the cylinder is determined by image segmentation. For the second approach, the inner volume of the cylinder is determined by coating the hollow cylinder with a very thin layer of waterproof spray paint and subsequent filling of the cylinder with water. Then, the mass of the water m_w is measured and converted into a volume.

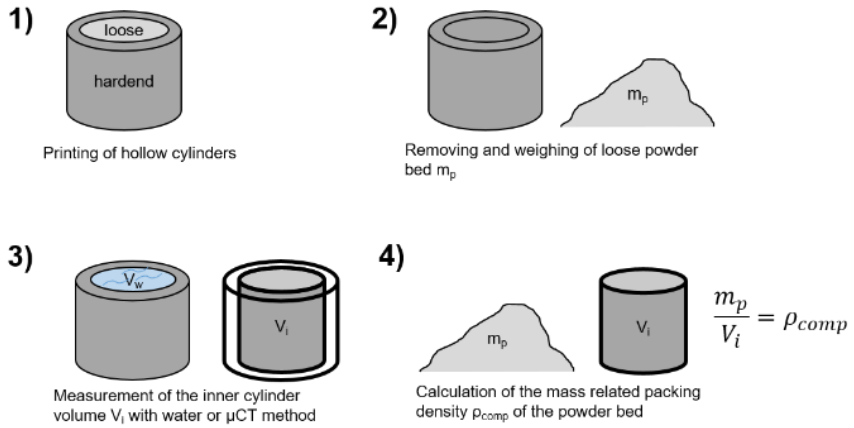

Figure 5: Schematic procedure of the measurement of the compacted powder bed density;

with the inner volume of the cylinder V_i (cm³) and the measured weight of the excavated material m_p (g) the mass-related packing density of the compacted particle bed ρ_{comp} (g/cm³) is calculated as follows:

$$\boldsymbol{\rho_{comp} = \frac{m_p}{V_i}} \qquad \text{Eq. 1}$$

When evaluating the methods, it was found that the results are comparable. Therefore, we recommend the water-filling method since it is time and resource efficient.

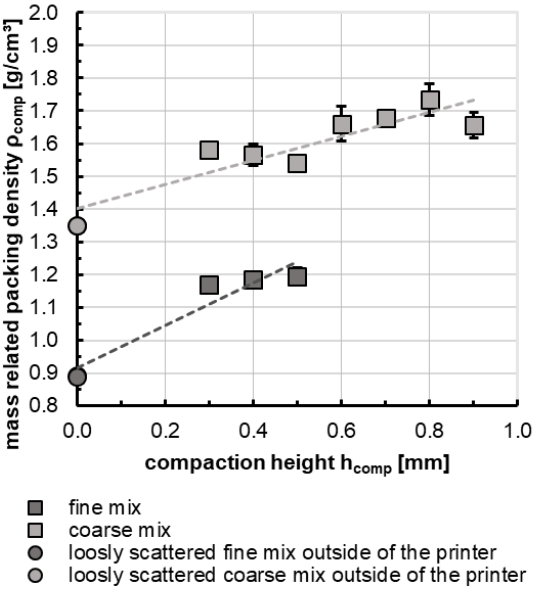

Figure 6: Effect of compaction height on the mass related particle bed packing density for a fine mix with d_{50} = 10 µm and a coarse mix with d_{50} = 230 µm for a layer height h_{lay} = 1 mm

Two particle bed mixtures containing cement (d_{50} = 9 µm) as well as a fine sand (d_{50} = 15 µm) or a coarse sand (d_{50} = 298 µm) with volumetric mixture ratios of sand/cement of 60/40 were tested. The mean material density was 2.80 g/cm³ for the fine mix and 2.79 g/cm³ for the coarse mix, respectively. The obtained packing densities of the particle bed for various compaction heights (h_{comp}) are shown in Figure 6 for a layer height h_{lay} = 1 mm. In addition, the loose density of the particle mixtures, i.e. without compaction, is shown, see solid circles in Figure 6. It is found that the packing density increases with increasing compaction height. In the fine mix the packing density is significantly lower than in the coarse mix. The highest packing density for the fine mix is measured at a compaction

height of 0.5 mm with 1.22 g/cm³. For the coarse particle bed mixture the packing density in the printer increases with compaction height from 1.57 g/cm³ for h_{comp} = 0.3 mm up to 1.66 g/cm³ for h_{comp} = 0.9 mm. Thus, based on a random loose packing measured outside of the printer (solid circles) the packing density increases by up to 33 % for the fine mix and 28 % for the coarse mix as a result of the compaction process in the printer. For the fine mix, the particle size of the cement (d_{50} = 9 µm) and the particle size of the fine aggregate (d_{50} = 16 µm) result in an almost monomodal particle packing. Thus, the voids in between the sand particles cannot be filled with cement particles. As a result, there are low packing densities [38], [39]. In the coarse mix, however, the fine cement particles fill the voids between the coarse sand particles (d_{50} = 298 µm) resulting in higher packing densities.

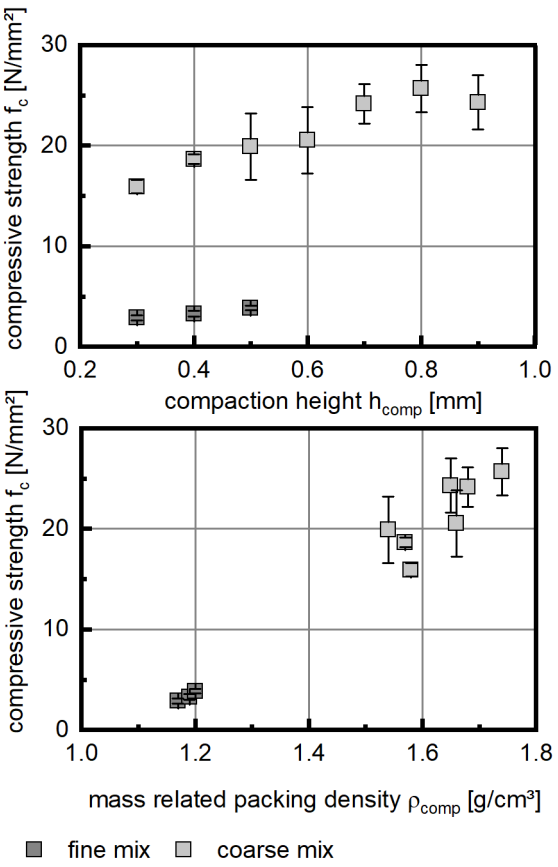

Figure 7: Compressive strength f_{c28d} of printed specimens depending on the compaction height and mass related packing density for w/c = 0.5 and q = 6 g/min

The effect of the level of compaction, i.e. the compaction height, on the mechanical strength of the specimens printed with a flowrate of q = 6 g/min and a w/c ratio of 0.5 is shown in Figure 7 top. Compressive strength tests were performed according to EN 12390-3 on the remaining halves of prisms 40 · 40 · 160 mm³ after a previously performed bending tensile test. The specimens were loaded orthogonally (90°) to the orientation of the layers. Before testing, the printed prisms were dry cut in order to enable plane parallel surfaces and to ensure an exact geometry. For both particle bed mixtures, the compressive strength increases with increasing compaction height. While the compressive strength for the fine mix increases slightly from 2.9 N/mm² to 3.8 N/mm², the compressive strength of the coarse mix is severely higher and ranges from 15.9 to 25.7 N/mm² for h_{comp} = 0.3 mm and 0.8 mm, respectively. This is a result of a denser particle bed with less porosity at high compaction levels, i.e. more particle contacts which improve the load transfer [39]. Accordingly, the compressive strength is increasing with increasing packing density,

see Figure 7 bottom. It is worth noting that along with the packing density, the cement content per 1m³ of printed concrete also increases. With a constant sand/cement volume ratio of 60/40 from 515 kg/m³$_{concrete}$ at a mass-related packing density of 1.2 g/cm³ to 687 kg/m³ at a mass-related packing density of 1.6 g/cm³. The resulting increased volume of hardened cement paste per 1m³ of printed concrete thus also plays a significant role in terms of increased strength.

Although an increase in compressive strength can be observed for high compaction levels, the quality of the printed specimens is quite diverse, see Figure 8. Cracks appear in the bottom of the printed specimens, increasing in number and size with increasing compaction height. This might be the result of the underlying hardening particle bed. When the cement starts to hydrate with water contact and the printed object gets stiffer in the lower layers, the high compaction on top induces a high tensile stress, which may damage the bottom layers, resulting in cracks.

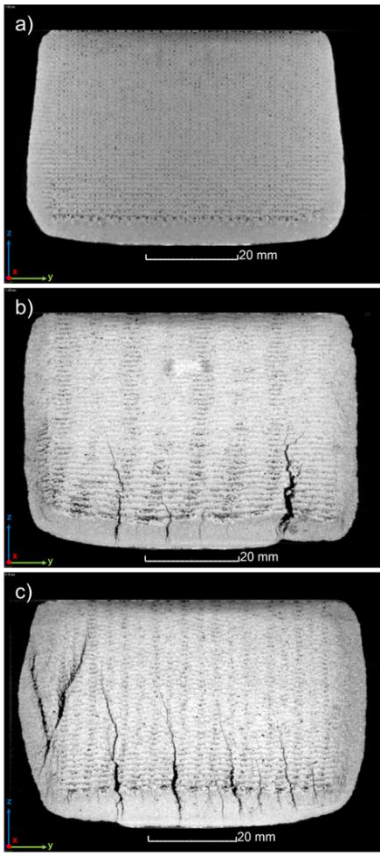

Figure 8: CT images of cross sections of printed cylinders with q = 6 g/min and w/c = 0.5, a) h_{comp} = 0.3 mm b) h_{comp} = 0.6 mm c) h_{comp} = 0.9 mm

These results show that the compaction process is of crucial importance for the mechanical properties of the printed components. Therefore, besides the compaction intensity, the effect of the location of the particle bed inside the printing area on the compaction was investigated using a Spectrum Z510 3D printing system with cementitious plaster materials produced by the company Z-Corp [40]. The printer can print components up to 356 mm (length) * 254 mm (width) * 203 mm (height). Again, the packing density of the powder bed was assessed in-situ by printing hollow containers with known internal volume [41]. Here, cubic containers with an inner side length of 20 mm and a wall thickness of 5 mm were used, see Figure 9 left. During printing, each layer of powder was spread and compacted by a roller with a diameter of 22 mm and a length of 356 mm. After printing, the containers were taken

out, and the mass of the unbound powder was measured. The packing density of the powder was then derived according to Eq. **1**.

It can be seen from Figure 9 right, that the packing density remains constant for the positions parallel to the roller (Y-axis). However, a decrease in powder packing density is found along the powder spreading direction (X-axis). According to the mathematical modelling in [42], the decrease in powder packing density along the powder spreading direction depends mainly on the powder excess displaced by the roller. It should be emphasised that the effect of a location-dependent packing density is related to the design of the printer and is therefore not a general phenomenon in particle bed 3D printing.

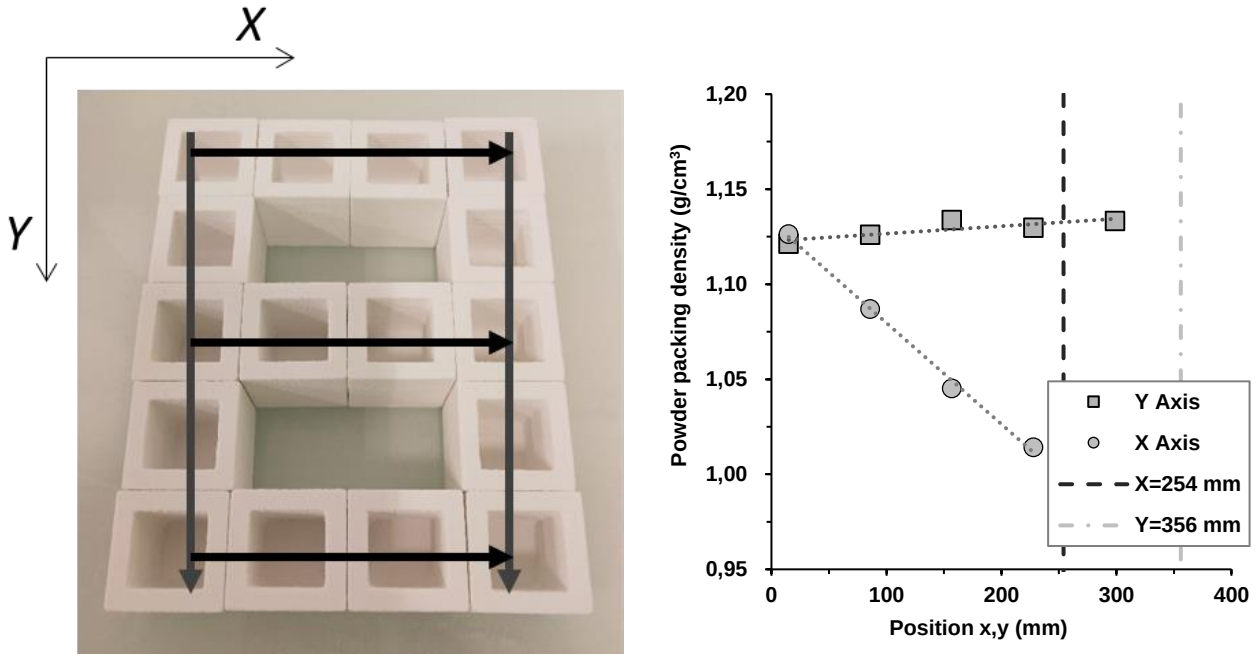

Figure 9: In-situ measurement of the packing density of the powder-bed printing: (left) Printed cubic shells as a powder container; (bright) Initial powder packing density as a function of position. Note: the X-axis (powder spreading direction) is bounded by the black dashed line; the Y axis (parallel to the roller axis) is bounded by the gray dash-dotted line.

2.2 Liquid application

In general, there are the two modes of liquid application in particle bed 3D printing: (1) continuous application of the liquid as a jet or (2) application as single droplets. In the second case, the liquid jet will break up into single droplets after a so called break up length. The mode of liquid application can significantly affect the mechanical as well as the geometrical properties of the printed components. Therefore, this effect should be both, quantifiable and controllable in the printing process.

Since a continuous liquid jet is prone to disturbances and is therefore favoring its disintegration into detached masses (droplets), the liquid jet usually breaks up after a certain time or length [43]–[45]. For a controlled application of the liquid as a droplet or a jet, the break up length is relevant with regard to the distance between nozzle and particle bed surface. The two most important process parameters affecting the breakup length are the nozzle diameter and the liquid flow rate. Therefore, the effect of these to parameters was investigated for cannulas with a diameter

of 100µm, 150µm and 220µm and flow rates of = 2, 3, 4, 5 and 6 g/min. Cannula diameter d and liquid flow rate q can be combined in the outlet velocity v:

$$v = \frac{q}{\pi(0.5d)^2} \quad \text{Eq. 2}$$

First, the effect of the flow rate and nozzle diameter, i.e. the outlet velocity, was experimentally investigated outside the 3D printer in a specifically designed test setup. In these experiments, the break up length was obtained by using a highspeed camera (Megaspeed, 2000 frames per second) and the image analysis software IC measure (The Imaging Source Europe, Bremen). The resulting break up length depending on the nozzle diameter and outlet velocities are shown in Figure 10. For the investigated range, the break up length varies between 0 cm for the lowest flow rate (150 µm and 220 µm, 2 g/min corresponding to 1.9 m/s and 0.9 m/s) and more than 2 cm for the smallest nozzle with the highest flow rate (100 µm, 5 g/min corresponding to 10.6 m/s). Two effects can be observed: (a) At constant cannula diameter, an increase in outlet velocity correlates linearly with an increase in break up length and (b) At constant outlet velocity, the larger the nozzle diameter, the higher the break up length.

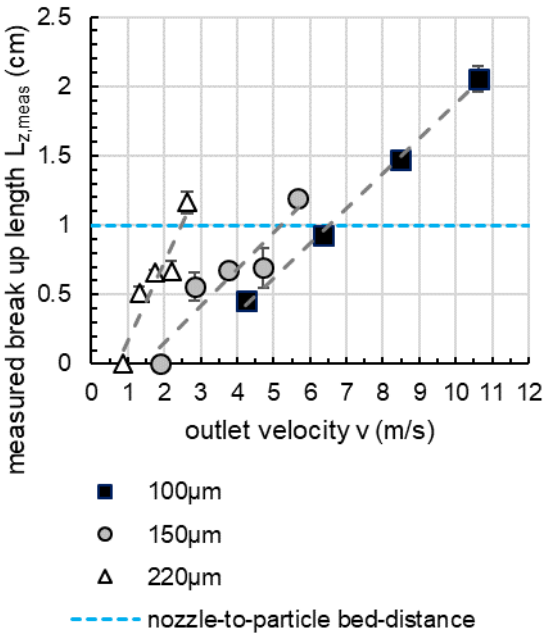

Figure 10: Break up length over outlet velocity for various nozzle diameters

The break up length L_Z can be approximated by a semi empirical-equation developed by Goldin et al. [46]. This equation enables to predict the break up length of a Newtonian liquid jet based on Rayleigh's linear stability theory [45] jet without induced wind:

$$L_Z = 12d[\sqrt{W_e} + 3\frac{W_e}{R_e}] \quad \text{Eq. 3}$$

With W_e (-) being the Weber number calculated with the density ρ (kg/m³), the velocity v (m/s), the diameter d (m) and the surface tension γ (N/m) according to:

$$W_e = \frac{\rho v^2 d}{\gamma} \quad \text{Eq. 4}$$

The Reynolds number R_e (-) is additionally considering the viscosity η and is computed from:

$$R_e = \frac{\rho v d}{\eta} \qquad \text{Eq. 5}$$

Based on Eq. 3 the break up length is calculated and compared to the measured break up length, Figure 11. As it is shown with the dashed line, in general, a good correlation of the calculated and measured break up length is prevalent, meaning that the relevant parameters are considered in the formula. However, the calculated break up length overestimates the measured break up length by 15% in average for the obtained data. Comparable trends were mentioned in [44].

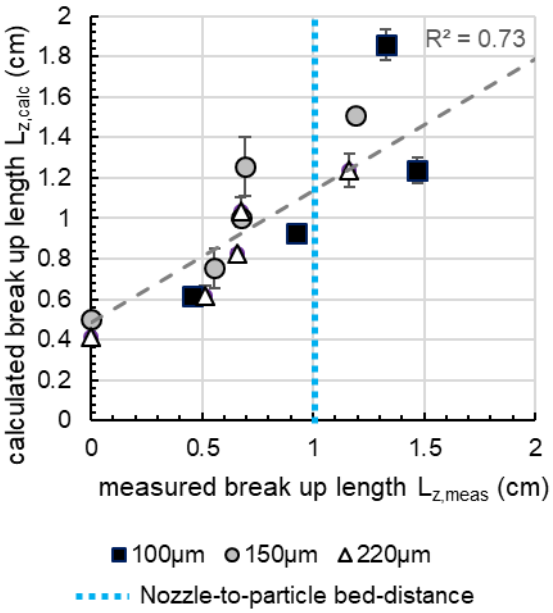

Figure 11: Comparison of calculated and measured break up length for nozzle diameters of 100µm, 150µm and 220µm.

In order to investigate the effect of the flow rate and the resulting mode of liquid application on the strength, specimens were produced in the 3D printer with a corresponding variation of the flow rate (2, 3, 4, 6, 9 g/min) using a nozzle diameter of 100 µm, see Figure 12. It is shown that an increase in flow rate from 2 g/min to 9 g/min increases the compressive strength of the printed objects from 14.8 MPa to 20.7 MPa. A particularly strong increase in compressive strength is observed when changing the liquid application regime from droplet to jet. The possible mechanisms underlying this are as follows:

(a) the jet enables a higher penetration depth of liquid in the particle bed, resulting in more homogenous liquid distribution within the particle bed and

(b) the particles are rearranged by the jet, resulting in a rougher surface of the particle bed. This roughness generates a higher mechanical interlocking between the layers, i.e. a higher interlayer bonding. This effect can be seen on the printed object's surface roughness, as it is exemplary shown for 2, 4 and 6 g/min in Figure 13. Here, the roughness of the printed surface was determined using a digital optical microscope (Keyence, VHX-2000D, magnification Z20x100). The higher the flow rates, the rougher the topography.

Thus, in order to ensure the liquid application as a jet for wide range of flow rates on the particle bed, smaller nozzle diameters are desirable.

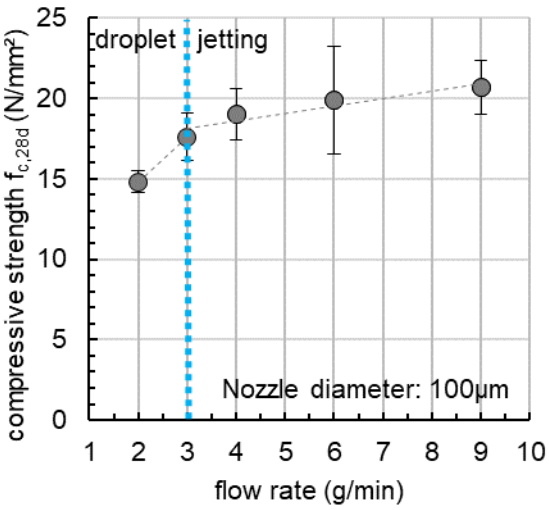

240

241 Figure 12: Effect of outlet velocity on compressive strength of printed specimen with a nozzle diameter of 100 µm

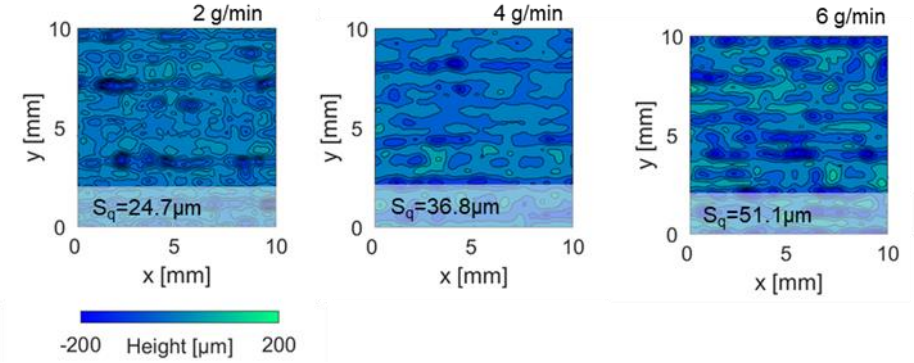

Figure 13: Surface contour plot from the top layer of specimen printed with 2g/min (left), 4g/min (middle) and 6g/min (rechts) with a nozzle diameter of 100µm and corresponding root mean square roughness S_q according to DIN EN ISO 25178-2

242

243 Besides the effect of the liquid application mode on the mechanical properties, it can also affect the dimensional
244 accuracy. In this context, a continuous jet is targeted. In contrast to individually deposited (dripped) droplets, a jet
245 enables a more precise liquid application onto the particle bed and thus a higher dimensional accuracy, see Figure
246 14.

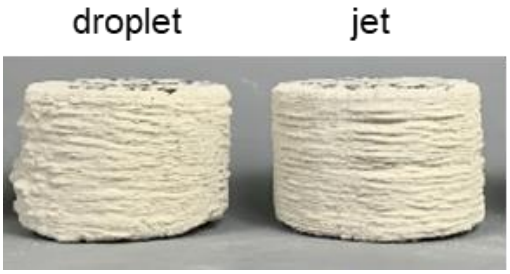

247

248 Figure 14: Comparison of printed cylinders (diameter: 60mm, height: 40mm) with droplet and liquid jet application

249

2.3 Liquid penetration in particle packings

2.3.1 Physics

In the Selective Cement Activation technique (SCA) the particle bed consists of fine aggregates, cement and where necessary admixtures. After liquid is applied, it is transported in the pores in between the particles. For a homogeneous hydration reaction within a layer and a good bond between the layers, the liquid has to to fully penetrate the individual layer of the particle bed. However, if too much liquid is used, it could spread beyond the target dimensions of the designated geometry, which would result in a low dimensional accuracy. Therefore, it is of merely importance to know the underlying mechanisms for the liquid intrusion into the particle bed.

In order to describe the liquid intrusion into the particle bed, the pores may be considered as a bundle of vertical capillaries. According to Washburn [47], the transported liquid volume is then equivalent to the intruded geometric pore space of n capillaries:

$$V = \pi \sum_{i=1}^{n} r^2 l \qquad \text{Eq. 6}$$

With r being the pore radius and l being the penetration length. In a particle bed the pore diameter is often expressed as a function of the particle diameter [48]–[50]. Depending on the packing density, the particle size distribution and shape, varying relations may be applied for estimating the pore radius, ranging from $0.2r_{particle} \leq r \leq r_{particle}$.

The volume flow $\dot{V}$ within these pores can be described in several ways, e.g. according to Darcy's law [51] or Hagen-Poiseuille's law [52]–[55]. The latter is expressed as follows and will be used further:

$$\dot{V} = \frac{dV}{dt} = \pi r^2 \frac{dl}{dt} = \frac{\pi r^4 \Delta p}{8 \mu l(t)} \qquad \text{Eq. 7}$$

With V being the intruding volume in a cylindrical capillary with radius r, t being the time, μ being the dynamic viscosity of the liquid and Δp being the driving pressure difference. The total pressure difference compromises three single pressure terms, the unbalanced atmospheric pressure p_{atm}, the hydrostatic pressure p_{hyd} and the capillary pressure p_{cap}:

$$\Delta p = \Delta p_{atm} + \Delta p_{hyd} + \Delta p_{cap} \qquad \text{Eq. 8}$$

For the boundary conditions in SCA, i.e. small pore radii and low penetration lengths with small liquid volumes, the atmospheric and hydrostatic pressure differences are smaller than the capillary pressure difference ($\Delta p_{atm} + \Delta p_{hyd} \ll \Delta p_{cap}$). Therefore, in simplified terms, the capillary pressure difference can be considered to be the main driving pressure, thus, making the Laplace-Equation become valid:

$$\Delta p \approx \Delta p_{cap} = \frac{2 \gamma cos \vartheta}{r} \qquad \text{Eq. 9}$$

With γ being the surface tension of the air/liquid interface and ϑ being the contact angle between the liquid and solid (particle). However, it needs to be pointed out that hydrostatic pressure may increase when printing several layers and could therefore become relevant when printing large objects and for fast vertical building rates.

When inserting Eq. 9, Eq. 7 becomes:

$$\frac{dl}{dt} = \frac{r\gamma cos\vartheta}{4\mu l(t)} \rightarrow l(t)dl = \frac{r\gamma cos\vartheta}{4\mu} \cdot dt \quad \text{Eq. 10}$$

After integration, the time depending penetration length $l(t)$ can be estimated with:

$$l(t) = \sqrt{\frac{r\gamma cos\vartheta}{2\mu} \cdot t} \quad \text{Eq. 11}$$

Since the particle bed can also be considered as a porous body [47], the penetration length can be also estimated based on the permeability K [52]:

$$l(t) = \sqrt{\frac{\Delta p_{cap} K t}{2\mu}} \quad \text{Eq. 12}$$

With Eq. 11 and Eq. 12 the main influencing factors on liquid penetration velocity in a particle bed can be derived:

- The pore size radius, i.e. particle size: The smaller the pores, the lower the penetration velocity. When assuming a correlation between pore radius and particle size distribution, finer particle systems are accompanied with lower intrusion velocities. Since the permeability K is i. a. linked to the pore size radius, compare e.g. [57], [58], the lower penetration velocity occurs also for particle beds with a lower permeability.
- Viscosity of the liquid: High liquid viscosities are accompanied with a lower penetration velocity.
- The contact angle between solid and liquid. The higher the contact angle, the lower the penetration velocity.

2.3.2 Liquid penetration with infinite water reservoir - Effect of particle size and particle reactivity

In order to experimentally prove the effect of particle size and reactivity, a setup was used to quantify capillary penetration in the presence of an infinite water reservoir. Therefore, particles are filled in a glass tube (diameter d_i = 23.5 mm), see Figure 14 middle top. The top of the tube is open, the bottom of the tube is covered with a lid with three holes (diameter d = 6 mm). A filter paper is used in order to prevent the particles from leaving the tube. The bottom of the glass tube is then put into a water reservoir and the subsequent fluid penetration from bottom to top over time is recorded starting from the water surface. The water volume in the reservoir was significantly larger than the pore volume of the particle bed in the glass tube, therefore the availability of water can be considered infinite. Although, the boundary conditions of the experiment do not directly describe the conditions during particle bed 3D printing - where a locally very limited applied water volume is prevalent - the described experimental setup provides valuable information on capillary flow within the particle bed.

Figure 15 left shows the experimentally determined penetration length over time $l(t)$ in a particle bed of different particle mixtures of aggregate (d_{50} = 298 µm) and cement (d_{50} = 9 µm) or ground limestone (d_{50} = 11 µm), compare supplementary material for particle size distribution. In order to vary the fineness of the mixture, we varied the amount of cement and ground limestone in the particle bed. A volumetric mix of aggregate/cement and aggregate/limestone of 80/40 (coarse, d_{50} = 276 µm) and 60/40 (fine, d_{50} = 230 µm) was used. When comparing the coarse particle beds (black symbols) with the fine particle beds (white symbols), a reduced penetration length over time is measured for the finer particle beds. Moreover, Figure 15 left illustrates that the particle beds containing

cement, i.e. a reactive component (triangular symbols) have a significantly lower penetration length over time than the non-reactive particle mixtures (squared symbols).

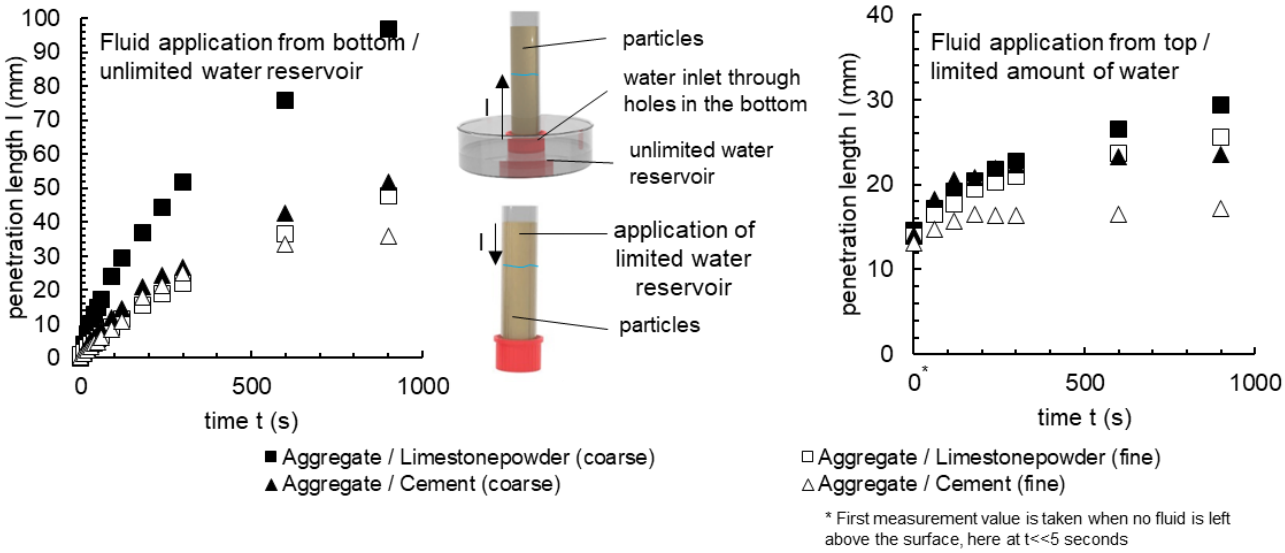

Figure 15: Measured water intrusion from bottom to top in a particle bed when an unlimited amount of liquid is prevalent (left) and from top to bottom with an limited amount of water (right) for two non-reactive (Aggregate/Limestone powder) and two reactive (Aggregate/cement) particle beds varying in their fineness (coarse (d_{50}=276µm)/fine (d_{50}=230µm))

2.3.3 Liquid penetration with limited water volume

At this point, however, it needs to be emphasized, that Eq. 11 is only valid for unlimited liquid reservoirs. However, in the printer only a limited amount of water is applied onto the particle bed in order to meet requirements regarding the water/cement-ratio per printed layer. Consequently, the effect of particle size and reactivity of the particles on liquid penetration was further investigated, also for a limited volume of water. Therefore, the glass tube (compare section 2.3.2) is filled with particles and 1.5 mL of fluid is homogeneously distributed on the particle's surface, Figure 15 middle bottom. The subsequent time depending fluid penetration process from top to bottom is recorded and evaluated over time. Thus, this experimental setup mimics the boundary conditions of water penetration during particle bed 3D printing.

The results clearly show a slower liquid penetration for a limited water volume, compare Figure 15 left (fully saturated pores) and right (unsaturated pores). The limited water volume results in unsaturated pores and a localized flow [59]. After the limited volume of water has completely penetrated the particle bed within a few seconds (compare section 2.3.4 and Figure 16), a "redistribution" of the water occurs with the result that the originally filled pores are drained. Due to the locally varying pore radii in the particle bed, pressure differences arise between the capillaries, compare Eq. 9. This causes a non-homogeneous intrusion behaviour of the liquid. If not all pores are fully saturated, the capillary flow is reduced compared to fully saturated pores. This finally results in a slower liquid penetration.

Thus, the limited amount of liquid as well as the presence of a reactive component determine liquid penetration behaviour into the particle bed significantly. This is shown in more detail in [60]–[62]. There, more precise modelling approaches are developed for the liquid penetration process into particle beds. Nevertheless, the importance of the parameters described before remains unchanged.

2.3.4 Liquid penetration in particle packings – Effect of cellulose ethers

Dimensional accuracy remains one of the primary concerns in particle bed binding techniques. As the liquid is free to spread in the particle bed, the final net geometry and surface roughness may be of relevance [14], [17], [27]. Ideally, the liquid is expected to move over a pre-determined and controlled length [14], [27], [40], [63]. Recent results show an effective way to ensure a controlled geometry of the resulting printed objects, incorporating thickeners for liquids such as cellulose ethers in the particle bed [61]. A one-dimensional penetration experiment was designed, using glass tubes (inner diameter = 10 mm) with cement powder packed inside (height = 100 mm) and distilled water (0.4 ml) added on the top of the particle bed. A digital camera was used to record the penetration length. The water penetration length was measured with time for various hydroxyethoxy methoxy cellulose (HEMC) mass dosages in a pure cement powder, see Figure 16. The HEMC used has a molar mass of 370,000 g/mol and a density of 1,200 kg/m^3. The degree of substitution and the molar substitution of HEMC are 1.5 and 0.20, respectively [64].

2.3.4.1 Polymer free and low polymer concentration

Saturated Penetration: For cement powder without or with low HEMC dosage (see 0 wt.% and 1 wt.% HEMC in Figure 16), water penetration length initially increases with the square root of time for around 1 min and slows down sharply afterwards. This transition occurs as the initial water on top of the sample has fully penetrated the cement packing. This situation corresponds to the so-called "saturation penetration length" assuming that water has fully saturated the porosity of the powder bed, see the fine dash line in Figure 16. Before reaching the saturation penetration length, i.e. as long as there is a reservoir of water above the surface, capillary-driven water penetration in the particle bed shall follow Lucas-Washburn law according to Eq. 11, [47], compare section 2.3.1. As previously mentioned, the penetration of water in a fine porous media is mainly capillary-driven since the capillary pressure p_{cap} is much higher than the hydrostatic pressure: $p_{cap} \gg \rho g H$. To evaluate this condition, a good approximation of p_{cap} is $2\gamma cos\vartheta / r$ (see Eq. 9). This condition holds true for most fine particle beds and the initial water penetration length in the particle bed scales therefore with the square root of time, see Figure 16.

Unsaturated Penetration: When there is no water left above the surface, the pores of the particle bed are expected to de-saturate as water penetration expends deeper in the powder. If the level of water saturation is assumed to remain uniform, the particle packing de-saturates homogeneously. The flow induced by capillary penetration strongly depends on permeability, which decreases with liquid saturation [65]. Thus, water penetration kinetics are expected to slow down sharply as the water reservoir above the cement packing vanishes. Moreover, the HEMC concentration in water should increase with the penetration length as the polymer gradually dissolves in the liquid, see 1 wt.% HEMC in Figure 16. This process increases the liquid viscosity and thus slows down the penetration. At longer time scales, as the HEMC concentration in the water further increases, the liquid becomes non-Newtonian and penetration fully stops (see next section).

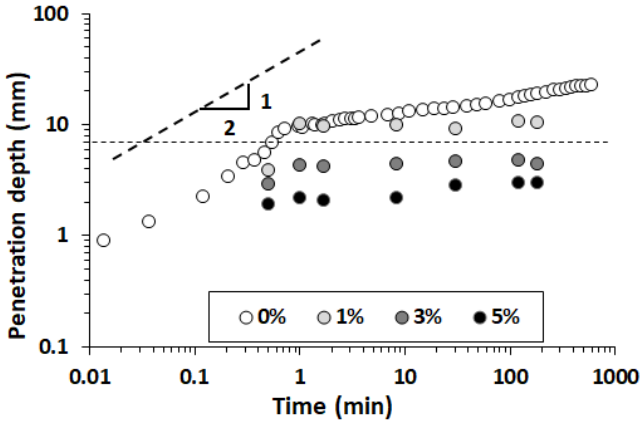

Figure 16. Penetration length as a function of time for particle beds containing different HEMC dosages. The numbers in the legend stand for the mass ratios of HEMC to cement [wt.%], the bold dash lines stand for the scaling relationship between penetration depth and time, and the fine dash line stands for the saturation penetration length after which the system is unsaturated, adapted from [61].

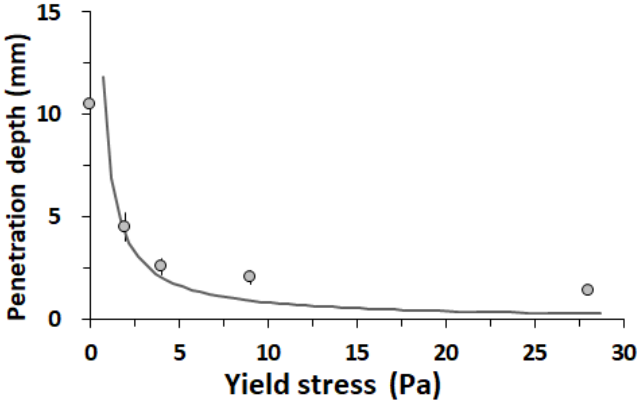

Figure 17. Experimental penetration length for penetrating liquid with a yield stress, compared to the theoretical penetration length adapted from [27].

2.3.4.2 High polymer concentration

For particle beds with high polymer dosage (3 wt.% and 5 wt.% HEMC in Figure 16), the penetration length stabilizes after a couple of minutes below the saturation penetration length. Thus, some water remains above the particle bed surface. As the liquid penetration stops early, this suggests that the penetrating liquid turns into a non-Newtonian liquid with a yield stress able to resist flow. According to [27], penetration is expected to stop as the yield stress of the penetrating liquid equilibrates the capillary gradient. Moreover, it should be noted that, for powder mixes with high HEMC dosages of 3 to 5 wt.%, the volume ratio of HEMC in the powder is around 8 to 13 vol.%. Given the constant packing density of powder mixes of around 30%, the amount of HEMC corresponds to 2.4 to 3.9 vol.% in the overall packing volume. When HEMC fully dissolves, the porosity increases thus by 2.4 to 3.9 vol.%, which can be neglected.

Furthermore, Figure 17 shows that the penetration length decreases with the yield stress. The predicted penetration depth is in good agreement with the measured depth for penetrating liquid with low yield stress. However, the experimental depth is higher than the predictive values for high HEMC dosage. This may be due to an over-estimation of the effective HEMC content in the penetrating liquid. Indeed, the cellulose ether dissolution, on such short time scales, may not be complete and the effective HEMC dosage shall then be lower than expected. This, in turn, reduces the effective yield stress of the liquid [66], [67].

Nevertheless, it appears clearly that, for systems where penetration depth stays in the saturated regime, the stabilized penetration depth decreases with the yield stress of the penetrating liquid. Higher effective cellulose concentration in the penetrating liquid leads to a better geometry control of the printed products.

2.3.5 Effect of cellulose ether on dimensional accuracy and strength

In order to determine the effect of methyl cellulose on the macroscopic properties of 3D printed elements, particle beds containing various amount of methyl hydroxyethyl cellulose in the dry mix (0, 0.5, 1, 1.5, 2, 2.5 wt.%) were investigated. The mechanical performance, i.e. compressive strength, was determined on halves of prisms with a

geometry of 40×40×160 mm³. To quantify the dimensional accuracy of printed objects, a shape index S_{3D} was determined, which compares the actually printed volume V_{act} [mm³] to the target volume V_{tar} [mm³]:

$$S_{3D} = \frac{V_{act}}{V_{tar}} \quad \text{Eq. 13}$$

If the actual fabricated geometry corresponds exactly to the designed dimensions, the shape index is 1. The higher the difference between the actual and design geometry, the higher the shape index and the lower the shape accuracy. Here, cylinders with a design diameter of 60 mm and a height of 40 mm were fabricated. The actual volume of the printed object was obtained by CT, as also described in [15].

The effect of methyl cellulose on the mechanical properties is shown in Figure 18. The addition of small amounts of methyl cellulose, increases the compressive strength of the printed specimens from 14.0 MPa (0 wt.% cellulose) up to 20.5 MPa (1.0 wt.% cellulose). However, adding more methyl cellulose reduces the compressive strength, as shown by the samples with 1.5 to 2.5 wt.%. The increase in methyl cellulose is accompanied by a linear decrease in density of the printed elements from 1.73kg/dm³ for 0 wt.% cellulose to 1.55kg/dm³ for 2.5 wt.% cellulose.

The increase in compressive strength at low dosages can be attributed to a temporary absorption and subsequent release of water, which may increase the degree of hydration in the vicinity of the methyl cellulose inclusions [15]. A delayed and slow provision of water to the cement in the particle bed could reduce the amount of evaporating water. This effect increases with an increase in methyl cellulose. However, at higher dosages of methyl cellulose, an antagonistic effect can also be observed. This can be attributed to a reduction in density with increasing methyl cellulose dosage and thus an increase in the porosity of the printed object. In addition, a reduction in the penetration length of the water (compare Figure 16) and an associated poor layer bonding could also contribute to the reduction in compressive strength at high dosages. Finally, it is also important that cellulose can cause a delay of cement hydration, which results in a delayed setting and hardening [68]–[74].

With regard to dimensional accuracy, an increase in methyl cellulose decreases the Shape Index S_{3D}, i.e increases the shape accuracy of printed objects, Figure 19. For methyl cellulose dosages up to 1.5 wt.% a decrease in Shape Index from 1.45 to 1.18 is observed. A further increase in methyl cellulose does not lead to a further decrease in Shape Index. An altered liquid penetration behavior in the particle bed containing methyl cellulose may occur mainly due to the water retention in the methyl cellulose inclusions. When water reaches the cellulose inclusion, it is partially and temporarily retained in the swelling methyl cellulose molecules. The more methyl cellulose available, the more water is stored. However, this water retention is a time depending process and therefore the Shape Index does not decrease further, if a certain cellulose dosage threshold is exceeded.

To summarize, the addition of methyl cellulose is an effective tool for printing objects with high dimensional accuracy and good mechanical performance. However, too high cellulose dosages do not lead to the desired effect, i.e. the compressive strength decreases without further decreasing the Shape Index. Therefore, a moderate amount - in this example 1-1.5 wt.% - is recommended for addition to the particle bed.

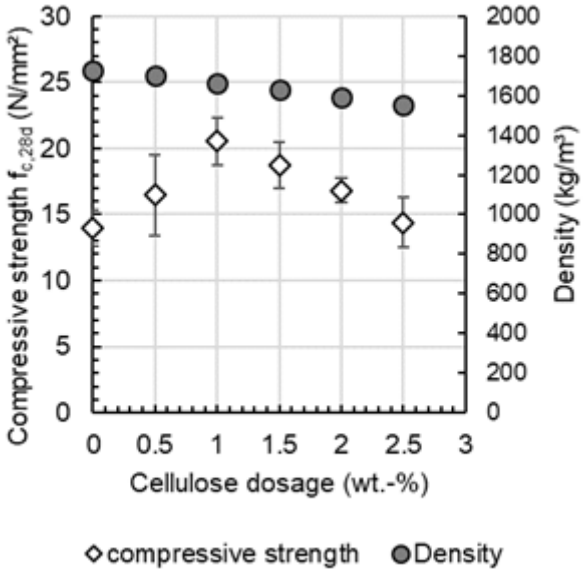

Figure 18. Effect of methyl cellulose dosage on compressive strength and on the density of printed objects

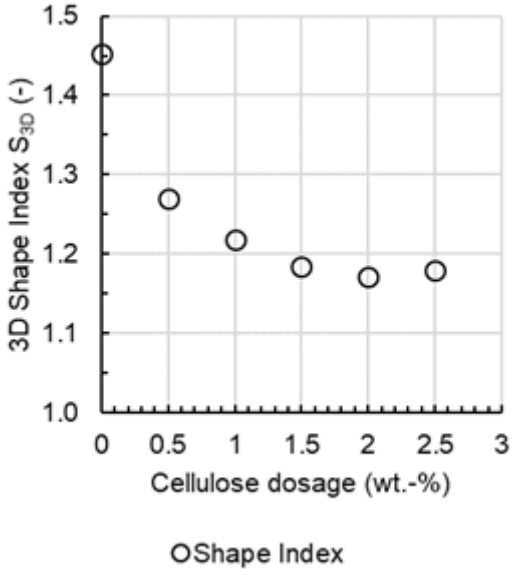

Figure 19. Effect of methyl cellulose dosage on Shape Index S_{3D} of printed objects

2.4 After finishing the printing process

2.4.1.1 Water evaporation

Evaporation inevitably occurs during and after the printing process as long as the printed elements are exposed to unsaturated air. Drying will reduce the final water content available for hydration of the powder bed. Figure 20 shows the relative mass loss of distilled water in a plaster (Z-Corp) and a cement (CEM I cement) particle bed in the condition of 22 ± 2°C and 35 % relative humidity. In this experiment, 12 to 15 water droplets were placed onto the particle bed and the mass was recorded every 5 seconds.

For plaster and cement particle beds, the relative water loss increases linearly with time until most of the water has evaporated, then the last fraction of water dries slowly or remains bound by hydration reactions. The setting time does appear as a noticeable transition time in the drying process, i.e. the slope of the curve changes as it can be seen at aprox. 30 min for plaster and approx.150 min for cement, [75]. At early age, the mass loss increases with the initial mass. Indeed, we suggest that the particle bed will lose water proportionally to the wetted surface, which increases with the mass, i.e. size of the water droplet, and the packing density of the particle bed. Therefore, water loss may be significant during printing if the time interval between water jetting on the consecutive layers is too long, and the drying rate is too high due to low relative humidity or high temperature.

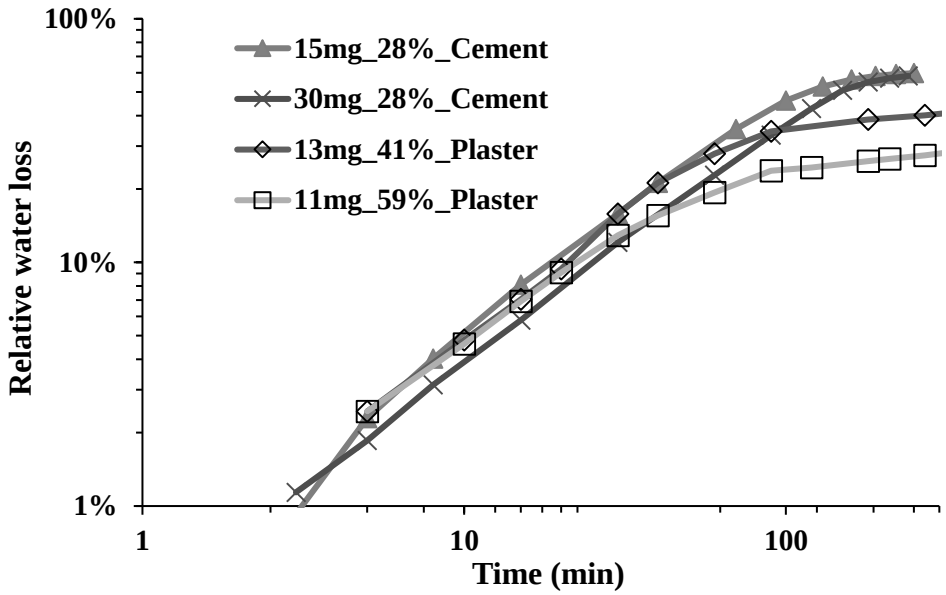

Figure 20. Relative water loss (i.e., the water loss divided by the initial water mass) as a function of evaporation time. Note: in the legend, the first value stands for the average mass of the droplets, the second value stands for the packing density of the powder-bed, the powder type is indicated in the third term.

2.4.1.2 After printing treatment

In the light of the significant evaporation during and after the printing process as well as the very low water content necessary for high dimensional accuracy, it is obvious that an after printing treatment by curing can be a useful option to increase the compressive strength, as shown for example by Xia et al. [16].

Figure 21 shows a comparison of the compressive strength for specimens with a w/c-ratio of 0.3. and 0.5, cured 7 d in tap water and a subsequently stored for 21 days at 20 °C and 65 % relative humidity, and specimens without any after printing treatment, i.e. stored for 28d at 20 °C and 65 % relative humidity immediately after the printing process. The after printing treatment, i.e. tap water curing, drastically increases the compressive strength by about 250 % to 25.9 N/mm² and 200 % to 28.5 N/mm² for specimens with a w/c-ratio of 0.3 and 0.5, respectively. Calorimetry measurements in Figure 22 show the remaining potential for hydration of the uncured specimens. In the experiment an uncured printed specimen, i.e. without after printing treatment, with a w/c-ratio of 0.5 and a specimen of the same w/c-ratio cured for 1 day in tap water were crushed to a particle size of approximately 0.1 mm and mixed with additional water in the measuring cell. The additional water content was chosen in such a way that a total water content of water applied during the printing process and water added for the calorimetry measurement would lead to a theoretical w/c-ratio of 3.33, which is significantly higher than would be necessary for the complete hydration of the unhydrated cement present in the sample. As expected, a much higher heat flow and generated heat can be observed for the specimen without after printing treatment. The difference between the curve of the uncured and the cured specimen can be interpreted as a kind of “after printing hydration potential”. Thus, looking at the difference in compressive strength of cured and uncured specimens water curing might be a promising way to utilise the full potential of SCA. For the production of components with thin cross-sections, this concept offers the possibility of

printing with a low w/c ratio and the associated high dimensional accuracy and then significantly improving the mechanical properties by after printing treatment.

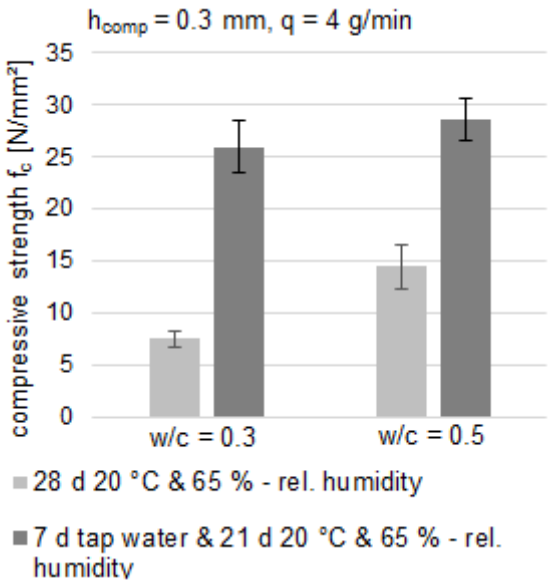

Figure 21: Compressive strength with and without after printing treatment

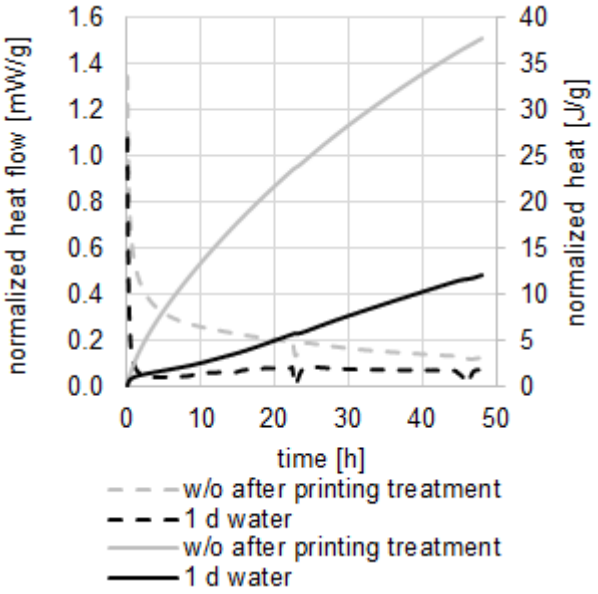

Figure 22: Calorimetry results of a specimen without after printing treatment and a specimen stored for 1d in tap water

3 Selective Paste Intrusion

3.1 Fluid application and penetration into the particle bed

3.1.1 Phenomenological effects and fundamental physics

In Selective Paste Intrusion, the typical size of the particles of the bed is of the order of around one millimetre. Therefore, the order of magnitude of the particle's mass is 1.4 mg. The particle stability is ensured by internal friction and the force needed to remove the particle can be computed assuming that the particle obeys to the Coulomb law and equals $m_{particle} \cdot g \cdot \tan\phi$ with ϕ being the internal friction angle of the particle bed (around 30°). In order to ensure that the particle bed is not shifted by the fluid deposition, this force has to be compared to the load induced by the deposition of the fluid. This latter force is induced by the kinetic energy of the cement paste hitting the particle bed and with $\rho_{fluid} \cdot V_{fluid} \cdot Q_{fluid}$ (where r_{fluid} (m) is the fluid density, V_{fluid} (m/s) is the fluid velocity and Q_{fluid} (m^3/s) is the fluid flow rate).

Contrarily to SCA, where a Newtonian liquid is applied, SPI uses very flowable cement pastes that displays a visco-plastic behaviour with a yield stress. The rheological behaviour of the penetrating fluid, i.e. the cementitious suspension, can be modelled using the Bingham model or the Herschel-Bulkley (HB) model [26], [28], [29], [76]. The constitutive equation of the latter is commonly written as:

$$\tau = \tau_0 + k\dot{\gamma}^n \qquad \text{Eq. 14}$$

where τ_0 (Pa) is the yield stress of the material, $\dot{\gamma}$ (s^{-1}) the shear rate, k ($Pa \cdot s^{-n}$) the consistency and n (-) the flow index of the HB model. Please note that the Bingham model is a particular case of the HB model, when $n = 1$. The driving principle of the SPI process is to rely on the material's yield stress to obtain the targeted penetration of the fluid. This means that the yield stress of the cement paste has to be fine-tuned in order to counterbalance the driving intrusion force and ensure that the penetration depth of the cement paste is equal to the height of the particle bed layers.

The basic theory used for the prediction of the penetration depth of the yield stress fluid through the particle bed layer is an adaptation of the one-dimensional Darcy law for a yield stress fluid displaying a HB type behaviour developed by Chevalier et al. [77]. The authors studied the steady state flow of a HB fluid through an assembly of particles of diameter D (m). The model is written in the non-linear form of the HB model and links the pressure drop per unit length ∇P ($Pa \cdot m^{-1}$) to the fluid penetration velocity using the fluid`s rheological parameter:

$$D\nabla P = \alpha\tau_0 + \beta k\left(\frac{V}{D}\right)^n \quad \text{Eq. 15}$$

where V is the fluid velocity ($m \cdot s^{-1}$), α and β are fitting parameters depending on the particles bed properties. Based on experimental results, Chevalier et al. [77] suggest values of 5.5 and 85 for α and β for an assembly of spherical particles.

The Chevalier equation is combined with the Green and Ampt approach to write the pressure drop in the particle bed over the penetrated depth Δh as a function of involved driving forces such as fluid initial kinetic energy ($0.5\rho V^2$), gravity (ρgH), capillary pressure ψ and friction effects λ that can be linked to the specific surface of the sand bed.

$$\nabla P(t) = \frac{1}{\Delta h(t)}\left[\rho g\left(H(t) + \frac{V^2}{2g}\right) + \psi - \lambda(t)\right] \quad \text{Eq. 16}$$

where H is the water head level (m). It is worth noting that with sand particles, the capillary effect (order of magnitude 10 Pa) can be neglected over gravity ρgH, which is at least one order of magnitude higher. The effect of the initial fluid velocity will depend on its magnitude.

Finally, it is of interest to predict the final penetration depth of the cement paste in the particle bed, i.e. the depth, where fluid intrusion velocity V decreases to zero. The calculation of the penetration depth is presented in the chapter 3.1.2. Ideally, the penetrated depth has to be equal to the height of the particle bed layer, as this achieves the highest mechanical strength without losing dimensional accuracy due to horizontal and vertical deviations of SPI-printed objects compared to the target geometry.

It should be mentioned that a deviation from the model prediction may occur due to the water absorption of dry sand particles. It is well known that in cementitious materials, aggregates can absorb a significant quantity of water (from few thousands to few percent of mass ratio). This absorption of water, that starts as soon as the cement paste becomes in contact with dry particles, tends to make the fluid stiffer by increasing its yield stress. Pierre et al. and Weger et al. have provided data proving that a preliminary wetting of the particle bed can be helpful to achieve higher penetration depths [76], [28].

3.1.2 *Model Implementation*

As described before, Chevalier et al. [77], [78] combined Darcy´s law and HB to model the flow of a yield stress fluid through a porous media of spheres (see Eq. 15 in section 3.1.1). Based on Chevalier's approach different models were created in [76] and [28] to model the penetration behaviour of cement pastes into particle beds.

Combining the Chevalier et al. approach with the Green and Ampt equations describing the penetration of a viscous fluid in an unsaturated particle bed [79], [80], Pierre et al. [76] developed a first model, in the following referred to as model A, for calculating the penetration depth of a cement paste into a particle bed. Following Eq. 15 the authors assumed that flow ($V > 0$) can only occur if Eq. 17 is fulfilled.

$$\nabla p > \frac{\alpha \cdot \tau_0}{D} \; or \; \tau_0 < \frac{D \cdot \nabla p}{\alpha} \qquad \text{Eq. 17}$$

The model of Pierre et al. has the form of Eq. 18, the derivation of the equations being found in [76]:

$$e_A = \frac{\rho_p \cdot g \cdot d_{50} \cdot (1-\varphi) \cdot h_{lay}}{\alpha \cdot \tau_0 - \rho_p \cdot g \cdot d_{50} \cdot \varphi + \frac{\varphi}{(1-\varphi)} \cdot 6 \cdot \tau_0 \cdot \kappa} \qquad \text{Eq. 18}$$

where e_A (m) is the penetration depth of the cement paste into the particle bed, ρ_p (kg · m^{-3}) is the density of the cement paste, g (m · s^{-2}) is the gravitational constant, d_{50} (mm) is the average particle size, φ (-) is the solid volume fraction of the particle bed, h_{lay} (m) is the height of the particle bed layer and κ (-) is the Janssen parameter [81] which describes the ratio of horizontal and vertical stresses, connected via the Poisson´s ratio ϑ_p. Furthermore, it is assumed that the cement paste is a largely incompressible medium and therefore $\vartheta_p = 0.5$ and $\kappa = 1$.

As will be pointed out later, model A shows good results with measured values but present some limitations. Due to the model's dependency on h_{lay}, it is only valid if the penetration depth ≤ layer thickness. Therefore, Weger et al. [28] suggest an adaptation of model A independent of h_{lay}. The authors described a final condition for the effective height of the cement paste that determines the initial effective hydrostatic pressure before penetrating the particle bed layer by using Eq. 19.

$$H_{0,eff} = \sqrt{\frac{\tau_0 \cdot 2 \cdot (b_{eff} - b_{nz})}{\rho_p \cdot g}} \qquad \text{Eq. 19}$$

where $H_{0,eff}$ (m) is the effective height of the cement paste determining the maximum initial hydrostatic pressure acting at the bottom of the cement paste, b_{eff} (m) is the final spread of the cement paste on the particle bed surface and b_{nz} (m) is the diameter of the nozzle.

By combining Eq. 18 and Eq. 19 model A+ is obtained. This model is now also valid for penetrations depths higher than the layer thickness of the particle bed, see Eq. 20.

$$e_{A+} = \frac{\rho_p \cdot g \cdot d_{50} \cdot H_{0,eff}}{\alpha \cdot \tau_0 + \frac{\varphi}{(1-\varphi)} \cdot 6 \cdot \tau_0 \cdot \kappa} \qquad \text{Eq. 20}$$

Model A and A+ assume an assembly of spherical particles and uses the value of fitting parameters α and β suggested by Chevalier et al.. In order to take into account the real morphology of the particle bed, Weger et al. [28] developed further models. Therefore, the authors suggest to model the particle bed as a capillary pores system in order to compute α and β values of Darcy´s law based on physical arguments, see Eq. 21 and Eq. 22.

$$\alpha \sim \frac{1}{\varepsilon} \quad \text{Eq. 21}$$

where α defines the penetration ability of a fluid, which depends on the widest path between the particles in the particle bed or on the porosity of the particle bed ε, respectively.

$$\beta \sim \frac{1}{\varepsilon \cdot \frac{\tau_0}{\tau_{0,\mathrm{lim}}}} \quad \text{Eq. 22}$$

where β describes the flow resistance of the entire particle bed as a function of pore size distribution and structure. Thus, β designates the mobilization of the fluid in the pores of the particle bed of porosity ε depending on the limiting yield stress $\tau_{0,\mathrm{lim}}$ (Pa) (depending on the pore size distribution and structure), see Eq. 23, as well as the actual yield stress of the fluid τ_0 (Pa).

$$\tau_{0,\mathrm{lim}} = \frac{\rho_p \cdot g \cdot H_{0,\mathrm{eff}} \cdot r_{\mathrm{eff}}}{2 \cdot L_{\mathrm{eff}}} \quad \text{Eq. 23}$$

where r_{eff} (m) is the effective radius of the capillary pore system of the particle bed according to Eq. 24 and L_{eff} (m) is the effective length of the capillary pores in the particle bed.

$$r_{\mathrm{eff}} = \left(\frac{8 \cdot G}{\pi}\right)^{\frac{1}{4}} \quad \text{Eq. 24}$$

where G can be calculated using Poiseuille's law $G = \chi \cdot A_{\mathrm{void}}^2 \cdot \frac{A_{\mathrm{void}}}{U_{\mathrm{void}}^2}$ and a form factor χ according to [82] as well as an assumption of an octahedral or tetrahedral shape of the void between the particles to calculate A_{void} (m^2) and U_{void} (m).

The combination of Eq. 21 and Eq. 22 with Eq. 15 (Darcy´s law and the Herschel-Bulkley model) leads to model D in Eq. 25. With their model D, the authors have developed a model that proves to be a very efficient prediction tool for fluids with low yield stress of less than 3 Pa:

$$e_D = \frac{\rho_p \cdot g \cdot \frac{H_{0,\mathrm{eff}}}{2} \cdot d_{\mathrm{eff}} \cdot \varepsilon}{\tau_0 + \frac{\tau_{0,\mathrm{lim}}}{\tau_0} \cdot k \cdot \dot{\gamma}^n} \quad \text{Eq. 25}$$

where $\dot{\gamma}$ (s^{-1}) is the shear rate of the penetrating cement paste in a pressure less capillary pore system and *n* is the Herschel-Bulkley flow index.

3.1.3 Comparing models and experimental data

The authors in [28] also conducted penetration tests with different cement pastes (w/c-ratio 0.30, 0.35 and 0.40, mini slump flow 400 mm) to compare the predictive capability of the models A+ and D. Both models showed accurate results especially in comparison with the penetration in a dry particle bed, see Figure 23 left. Furthermore, the results show the positive effect of the calculation of the α and β values especially for cement pastes with low yield stress, i.e. high mini slump flow. Additionally, model D seems to be able to reproduce the effect of an increasing w/c-ratio, see Figure 23 right.

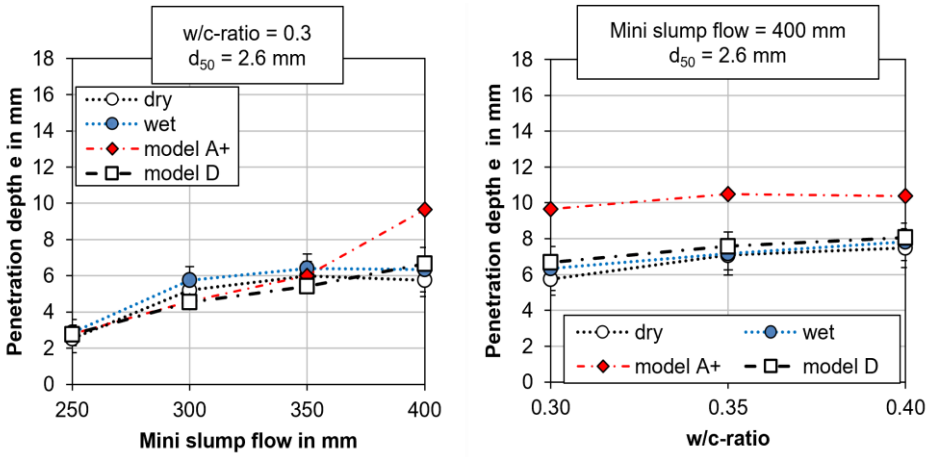

Figure 23: Penetration depth of a cement paste in dependence of flowability (left) and w/c-ratio (right) in a particle bed with an average particle size of 2.6 mm [28].

3.2 Macroscopic material properties

Weger and Gehlen [83] provide an overview of strength and durability properties of SPI material (w/c-ratio 0.3, d_{50} = 1.6 mm, layer thickness 3 mm). These researchers have reported compressive strength values up to 78 MPa after 7d and good durability properties in terms of carbonation resistance, chloride penetration resistance as well as freeze-thaw resistance, i.e. XC4, XS2/XD2 and XF3/XF4 according to EN 206, independent of the layer orientation (results not shown here). Furthermore, the compressive strength values show a clear dependency on the density of the printed samples and therefore a comparable behaviour to conventional casted concrete, compare REF in Figure 24. The increase in density is attributed to a reduced air void content in the manufactured samples, which is associated with an increasing amount of paste and a resulting higher pore filling of the particle bed.

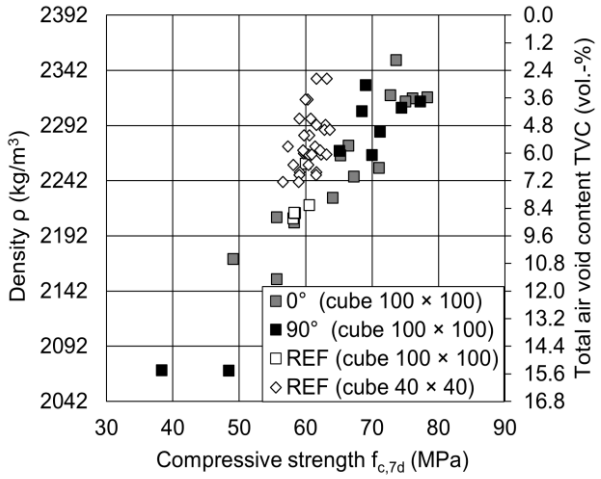

Figure 24: Compressive strength in dependency of the density, 0° = load parallel to the layers, 90° = load perpendicular to the layers, dimensions of the test specimens in the brackets in mm [83].

4 Conclusions

In this paper, we have discussed in detail the material-process interactions and their underlying physics in the particle bed binding techniques of Selective Cement Activation and Selective Paste Intrusion. Due to the specific

characteristics of particle bed binding - with the separate creation of a particle bed layer and the subsequent selective binding - the consideration of the effects and interactions of material and process is of particular importance. Therefore, we considered the most relevant parameters in the individual sub-processes.

In **Selective Cement Activation**, the focus was on particle layer compaction, fluid application, fluid penetration and after printing treatment. We have proven that an increase in packing density of the particle bed can be achieved via compaction in the printer and increases the compressive strength of the printed objects. With regard to fluid application, it was possible to show that an increase in flow rate also increases the compressive strength. This phenomenon can be attributed to a higher penetration depth of the liquid as well as a rougher particle bed surface, which is assumed to result in a higher mechanical interlocking between the layers, i.e. a higher interlayer bonding.

For fluid penetration, we showed that a reduced penetration length over time is measured for finer particle beds as well as for particle beds containing cement, i.e. a reactive component. The underlying mechanisms were described and discussed by means of physically based material models. Furthermore, we showed that the addition of cellulose ether also leads to a reduced penetration length. Macroscopically, increased cellulose ether contents lead to an increase in the dimensional accuracy of the printed elements. However, the compressive strength only increases up to medium cellulose ether content and then decreases again as the contents increase further.

Last but not least, we could demonstrate that an after-printing treatment by water curing leads to a significant increase of the mechanical properties. This can primarily be attributed to an activation of the hydration potential of the cement, which was not fully exploited by the Selective Cement Activation process before.

In the 3D printing process of **Selective Paste Intrusion**, the primary focus was on the penetration of the cement paste into the particle bed. Various models that capture the rheology of the cement paste on the one hand and the properties of the particle bed on the other were derived based on Chevalier´s approach and evaluated in terms of their predictive accuracy. We have shown that with increasing filling of the voids of the particle bed with cement paste, i.e. with increasing bulk density, there is an increase in the compressive strength of the printed specimens. Furthermore, good durability properties in terms of carbonation resistance, chloride penetration resistance as well as freeze-thaw resistance were reported for specimen produced with Selective Paste Intrusion.

Finally, we can conclude that the manifold material-process interactions represent a major challenge for the reliable control of particle bed 3D printing, however, they also offer many opportunities to control the material properties of the printed elements in a systematic manner.

5 Acknowledgements

The authors gratefully acknowledge the funding by the German Research Foundation (DFG, Project No 389705984 and 414265976 with project A01) as well as the European funding for the regions in Lower Saxony (EFRE)/NBank within the project “RheoStruc^{3D} Lab” (85023242) for funding the Particle bed 3D-printer. Furthermore this research was funded by ZukunftBau, grant number SWD-10.08.18.7-21.19.

6 References

[1] I. Agustí-Juan, A. Jipa, and G. Habert, “Environmental assessment of multi-functional building

elements constructed with digital fabrication techniques," *Int. J. Life Cycle Assess.*, vol. 24, no. 6, pp. 1027–1039, Jun. 2019, doi: 10.1007/s11367-018-1563-4.

[2] M. Rippmann, A. Liew, T. Van Mele, and P. Block, "Design, fabrication and testing of discrete 3D sand-printed floor prototypes," *Mater. Today Commun.*, vol. 15, pp. 254–259, Jun. 2018, doi: 10.1016/j.mtcomm.2018.03.005.

[3] G. De Schutter, K. Lesage, V. Mechtcherine, V. N. Nerella, G. Habert, and I. Agusti-Juan, "Vision of 3D printing with concrete — Technical, economic and environmental potentials," *Cem. Concr. Res.*, vol. 112, pp. 25–36, Oct. 2018, doi: 10.1016/j.cemconres.2018.06.001.

[4] H. Kloft *et al.*, "TRR 277: Additive manufacturing in construction," *Civ. Eng. Des.*, vol. 3, no. 4, pp. 113–122, Sep. 2021, doi: 10.1002/cend.202100026.

[5] F. Craveiro, H. M. Bartolo, A. Gale, J. P. Duarte, and P. J. Bartolo, "A design tool for resource-efficient fabrication of 3d-graded structural building components using additive manufacturing," *Autom. Constr.*, vol. 82, pp. 75–83, Oct. 2017, doi: 10.1016/j.autcon.2017.05.006.

[6] F. Bos, R. Wolfs, Z. Ahmed, and T. Salet, "Additive manufacturing of concrete in construction: potentials and challenges of 3D concrete printing," *Virtual Phys. Prototyp.*, vol. 11, no. 3, pp. 209–225, Jul. 2016, doi: 10.1080/17452759.2016.1209867.

[7] K. Dörfler, G. Dielemans, L. Lachmayer, A. Raatz, D. Lowke, and M. Gerke, "Additive Manufacturing Using Mobile Robots: Opportunities and Challenges for Building Construction," *Cem. Concr. Res.*, no. this issue, 2022.

[8] K. Kuzmenko, N. Ducolombier, A. Feraille, and N. Roussel, "EMBODIED AND OPERATIONAL CONTRIBUTION TO CLIMATE-CHANGE OF A CONCRETE-PRINTING ROBOTIC CELL - GENERIC MODEL, POWER MEASUREMENTS AND INFLUENCE OF PRINTING RESOLUTION," *Cem. Concr. Res.*, no. this issue, 2022.

[9] G. Ma, R. Buswell, W. R. L. da Silva, L. Wang, J. Xub, and S. Jones, "Technology readiness: a global snapshot of 3D concrete printing and the frontiers for development," *Cem. Concr. Res.*, no. this issue, 2022.

[10] F. P. Bos *et al.*, "The Realities of Additively Manufactured Concrete Structures in Practice," *Cem. Concr. Res.*, no. this issue, 2022.

[11] H. Kloft *et al.*, "TRR 277: Additive Fertigung im Bauwesen," *Bautechnik*, 2021, doi: 10.1002/bate.202000113.

[12] R. A. Buswell *et al.*, "A process classification framework for defining and describing Digital Fabrication with Concrete," *Cem. Concr. Res.*, vol. 134, p. 106068, Aug. 2020, doi: 10.1016/j.cemconres.2020.106068.

[13] R. A. Buswell *et al.*, "Digital Fabrication with Cement-Based Materials: Process Classification and

644 Case Studies," in *Digital Fabrication with Cement-Based Materials*, R. N.; and L. D., Eds. Cham:
645 Springer, 2022, pp. 11–48.
646 [14] D. Lowke, E. Dini, A. Perrot, D. Weger, C. Gehlen, and B. Dillenburger, "Particle-bed 3D printing
647 in concrete construction – Possibilities and challenges," *Cem. Concr. Res.*, vol. 112, no. November
648 2017, pp. 50–65, 2018, doi: 10.1016/j.cemconres.2018.05.018.
649 [15] D. Lowke *et al.*, "Particle bed 3D printing by selective cement activation – Applications, material
650 and process technology," *Cem. Concr. Res.*, vol. 134, no. April, p. 106077, 2020, doi:
651 10.1016/j.cemconres.2020.106077.
652 [16] M. Xia, B. Nematollahi, and J. Sanjayan, "Post-processing Techniques to Enhance Strength of
653 Portland Cement Mortar Digitally Fabricated Using Powder-Based 3D Printing Process," *RILEM*
654 *Bookseries*, vol. 23, no. 1, pp. 457–464, 2020, doi: 10.1007/978-3-030-22566-7_53.
655 [17] P. Shakor, S. Nejadi, G. Paul, and J. Sanjayan, "Dimensional accuracy, flowability, wettability, and
656 porosity in inkjet 3DP for gypsum and cement mortar materials," *Autom. Constr.*, vol. 110, no.
657 December 2019, p. 102964, 2020, doi: 10.1016/j.autcon.2019.102964.
658 [18] P. Shakor, J. Sanjayan, A. Nazari, and S. Nejadi, "Modified 3D printed powder to cement-based
659 material and mechanical properties of cement scaffold used in 3D printing," *Constr. Build. Mater.*,
660 vol. 138, pp. 398–409, May 2017, doi: 10.1016/j.conbuildmat.2017.02.037.
661 [19] D. Talke, Daniel; Henke, Klaudius; Weger, "Selective Cement Activation (SCA) – new possibilities
662 for additive manufacturing in construction," in *Proceedings of IASS Annual Symposia, IASS 2019*
663 *Barcelona Symposium: Advanced Manufacturing and Non-conventional Materials*, 2019, pp. 1–8,
664 [Online]. Available:
665 https://www.ingentaconnect.com/content/iass/piass/2019/00002019/00000006/art00011#Refs.
666 [20] D. Lowke, D. Weger, K. Henke, D. Talke, S. Winter, and C. Gehlen, "3D-Drucken von
667 Betonbauteilen durch selektives Binden mit calciumsilikatbasierten Zementen–Erste Ergebnisse zu
668 beton-technologischen und verfahrenstechnischen Einflüssen," in *ibausil*, 2015, vol. 1, pp. 1113–
669 1120.
670 [21] J. Ingaglio, J. Fox, C. J. Naito, and P. Bocchini, "Material characteristics of binder jet 3D printed
671 hydrated CSA cement with the addition of fine aggregates," *Constr. Build. Mater.*, vol. 206, pp.
672 494–503, May 2019, doi: 10.1016/j.conbuildmat.2019.02.065.
673 [22] G. Cesaretti, E. Dini, X. De Kestelier, V. Colla, and L. Pambaguian, "Building components for an
674 outpost on the Lunar soil by means of a novel 3D printing technology," *Acta Astronaut.*, vol. 93, pp.
675 430–450, Jan. 2014, doi: 10.1016/j.actaastro.2013.07.034.
676 [23] P. Shakor, N. Gowripalan, and H. Rasouli, "Experimental and numerical analysis of 3D printed
677 cement mortar specimens using inkjet 3DP," *Arch. Civ. Mech. Eng.*, vol. 21, no. 2, p. 58, May 2021,

678 doi: 10.1007/s43452-021-00209-3.
679 [24] A. Fuente, A. Blanco, E. Galeote, and S. Cavalaro, “The first 3D-printed concrete footbridge in
680 Spain,” *Cem. Concr. Res.*, no. this issue, 2022.
681 [25] D. Weger, D. Lowke, and C. Gehlen, “3D printing of concrete structures using the selective binding
682 method – Effect of concrete technology on contour precision and compressive strength,” 2016.
683 [26] A. Pierre, D. Weger, A. Perrot, and D. Lowke, *2D Numerical Modelling of Particle-Bed 3D Printing
684 by Selective Paste Intrusion*, vol. 28. 2020.
685 [27] A. Pierre, D. Weger, A. Perrot, and D. Lowke, “Penetration of cement pastes into sand packings
686 during 3D printing: analytical and experimental study,” *Mater. Struct. Constr.*, vol. 51, no. 1, p. 22,
687 Feb. 2018, doi: 10.1617/s11527-018-1148-5.
688 [28] D. Weger, A. Pierre, A. Perrot, T. Kränkel, D. Lowke, and C. Gehlen, “Penetration of Cement Pastes
689 into Particle-Beds: A Comparison of Penetration Models,” *Materials (Basel).*, vol. 14, no. 2, p. 389,
690 Jan. 2021, doi: 10.3390/ma14020389.
691 [29] A. Pierre, D. Weger, A. Perrot, and D. Lowke, “Additive Manufacturing of Cementitious Materials
692 by Selective Paste Intrusion: Numerical Modeling of the Flow Using a 2D Axisymmetric Phase
693 Field Method,” *Materials (Basel).*, Nov. 2020, doi: 10.3390/ma13215024.
694 [30] D. Weger, D. Lowke, C. Gehlen, D. Talke, and K. Henke, “Additive manufacturing of concrete
695 elements using selective cement paste intrusion–effect of layer orientation on strength and
696 durability,” in *Proceedings of RILEM 1st International Conference on Concrete and Digital
697 Fabrication*, 2018, pp. 10–12.
698 [31] I. Mai *et al.*, “Large Particle 3D Concrete Printing—A Green and Viable Solution,” *Materials
699 (Basel).*, vol. 14, no. 20, p. 6125, Oct. 2021, doi: 10.3390/ma14206125.
700 [32] S. Yu, H. Du, and J. Sanjayan, “Aggregate-bed 3D concrete printing with cement paste binder,”
701 *Cem. Concr. Res.*, vol. 136, p. 106169, Oct. 2020, doi: 10.1016/j.cemconres.2020.106169.
702 [33] A. Jipa and B. Dillenburger, “3D Printed Formwork for Concrete: State-of-the-Art, Opportunities,
703 Challenges, and Applications,” *3D Print. Addit. Manuf.*, Sep. 2021, doi: 10.1089/3dp.2021.0024.
704 [34] B. Dillenburger, R. Flatt, and J. Schwartz, “Smart Slab.” https://dfabhouse.ch/smart-slab/.
705 [35] Progress, “3D printing in a new dimension,” 2021. .
706 [36] A. Budding and T. H. J. Vaneker, “New strategies for powder compaction in powder-based rapid
707 prototyping techniques,” *Procedia CIRP*, vol. 6, pp. 527–532, 2013, doi:
708 10.1016/j.procir.2013.03.100.
709 [37] B. Liu, R. Wildman, C. Tuck, I. Ashcroft, and R. Hague, “Investigaztion the effect of particle size
710 distribution on processing parameters optimisation in selective laser melting process,” *22nd Annu.
711 Int. Solid Free. Fabr. Symp. - An Addit. Manuf. Conf. SFF 2011*, pp. 227–238, 2011.

[38] F. de Larrard, *Concrete mixture proportioning: A scientific approach*, vol. 9. 1999.

[39] H.-G. Kessler, "Kessler_1994_Kugelmodell für Ausfallkörnugen dichter Betone.pdf," *Betonw. + Fert.*, vol. 11, pp. 63–76, 1994.

[40] P. Feng, X. Meng, J. F. Chen, and L. Ye, "Mechanical properties of structures 3D printed with cementitious powders," *Constr. Build. Mater.*, vol. 93, pp. 486–497, 2015, doi: 10.1016/j.conbuildmat.2015.05.132.

[41] A. M. Elliott, P. Nandwana, D. Siddel, and B. G. Compton, "A method for measuring powder bed density in binder jet additive manufacturing process and the powder feedstock characteristics influencing the powder bed density," in *Solid Freeform Fabrication 2016: Proceedings of the 27th Annual International Solid Freeform Fabrication Symposium - An Additive Manufacturing Conference, SFF 2016*, 2016, pp. 1031–1037.

[42] Y. Shanjani and E. Toyserkani, "Material spreading and compaction in powder-based solid freeform fabrication methods: Mathematical modeling," in *19th Annual International Solid Freeform Fabrication Symposium, SFF 2008*, 2008, pp. 399–410.

[43] Y. A. Haenlein, "Ueber den Zerfall eines FIuessigkeitsstrahles," *Forsch. auf dem Gebiet des Ingenieurwesens A*, vol. 4, no. April, pp. 139–149, 1931.

[44] B. Bonhoeffer, A. Kwade, and M. Juhnke, "Impact of Formulation Properties and Process Parameters on the Dispensing and Depositioning of Drug Nanosuspensions Using Micro-Valve Technology," *J. Pharm. Sci.*, vol. 106, no. 4, pp. 1102–1110, 2017, doi: 10.1016/j.xphs.2016.12.019.

[45] Lord Rayleigh, "On The Instability Of Jets," *Proc. London Math. Soc.*, vol. 14, no. June 1873, pp. 4–13, 1878.

[46] R. Goldin, M.; Pfeffer, R.; Shinnar, "Break-up of a capillary jet of a non-Newtonian fluid having a yield stress," *Chem. Eng. J.*, vol. 1, no. 4, pp. 8–20, 1972.

[47] E. W. Washburn, "The Dynamics of Capillary Flow," *Phys. Rev.*, vol. 17, no. 273, pp. 273–283, 1921, doi: 10.1103/PhysRev.17.273.

[48] M. M. Roozbahani, R. Borela, and J. D. Frost, "Pore size distribution in granular material microstructure," *Materials (Basel).*, vol. 10, no. 11, pp. 1–21, 2017, doi: 10.3390/ma10111237.

[49] C. Marliere, E. Mabrouk, M. Lamblet, and P. Coussot, "How water retention in porous media with cellulose ethers works," *Cem. Concr. Res.*, vol. 42, no. 11, pp. 1501–1512, 2012, doi: 10.1016/j.cemconres.2012.08.010.

[50] L. Gao, Shengyan; Meegoda, Jay N.; Hu, "Two methods for pore network of porous media," *Int. J. Numer. Anal. Methods Geomech.*, vol. 36, no. 18, pp. 1954–1970, 2012, doi: 10.1002/nag.1134.

[51] H. Darcy, *Les fontaines publiques de la ville de Dijon*. 1856.

[52] G. Hagen, “Ueber die Bewegung des Wassers in engen cylindrischen Röhren,” pp. 423–443, 1839.

[53] E. Hagenbach, *Ueber die Bestimmung der Zähigkeit einer Flüssigkeit durch den Ausfluss von Roehren*. Pogendorf’s Annalen der Physik und Chemie 108 (Reprinted 1933 in Schiller), 1860.

[54] L. Schiller, *Drei Klassiker der Strömungslehre: Hagen, Poiseuille, Hagenbach*. 1933.

[55] W. H. Poiseuille, J. L. M.; Herschel, *Experimental investigations upon the flow of liquids in tubes of very small diameter*. Lancester: Lancester Inc, 1940.

[56] W. Zuo, C. Dong, E. Keita, and N. Roussel, “Penetration Study of Liquid in Powder Bed for 3D Powder-Bed Printing,” in *Second RILEM International Conference on Concrete and Digital Fabrication 2020*, T. Bos, F.; Lucas, S.; Wolfs, R.; Salet, Ed. 2020, pp. 379–386.

[57] P. C. Carman, “Permeability of saturated sands, soils and clays,” *J. Agric. Sci.*, vol. 29, no. 2, pp. 262–273, 1939, doi: 10.1017/S0021859600051789.

[58] J. Kozeny, “Uber kapillare Leitung der Wasser in Boden,” *Sitzungsber. Akad. Wiss. Wien*, vol. 136, pp. 271– 306, 1927.

[59] C. M. Boyce, A. Ozel, and S. Sundaresan, “Intrusion of a Liquid Droplet into a Powder under Gravity,” *Langmuir*, vol. 32, no. 34, pp. 8631–8640, 2016, doi: 10.1021/acs.langmuir.6b02417.

[60] A. Mai, I.; Lowke, D.; Perrot, “Fluid intrusion in powder beds for selective cement activation – an experimental and analytical study,” *Cem. Concr. Res.*, vol. submitted, 2021.

[61] W. Zuo, C. Dong, P. Belin, N. Roussel, and E. Keita, “Capillary imbibition depth in particle-bed 3D printing – physical frame and onedimensional experiments,” *submitted*, 2021.

[62] T. Mauffré, E. Keita, E. Contraires, F. McGregor, and A. Fabbri, “Analysis of water droplet penetration in earth plasters using X-ray microtomography,” *Constr. Build. Mater.*, vol. 283, p. 122651, May 2021, doi: 10.1016/j.conbuildmat.2021.122651.

[63] M. Xia, B. Nematollahi, and J. Sanjayan, “Printability, accuracy and strength of geopolymer made using powder-based 3D printing for construction applications,” *Autom. Constr.*, vol. 101, pp. 179–189, 2019, doi: 10.1016/j.autcon.2019.01.013.

[64] C. Brumaud *et al.*, “Cellulose ethers and water retention,” *Cem. Concr. Res.*, vol. 53, pp. 176–184, 2013, doi: 10.1016/j.cemconres.2013.06.010.

[65] F. Osselin, A. Fabbri, T. Fen-Chong, J. M. Pereira, A. Lassin, and P. Dangla, “Experimental investigation of the influence of supercritical state on the relative permeability of Vosges sandstone,” *Comptes Rendus - Mec.*, vol. 343, no. 9, pp. 495–502, 2015, doi: 10.1016/j.crme.2015.06.009.

[66] F. Lequeux, L. Talini, E. Verneuil, G. Delannoy, and P. Valois, “Wetting of polymers by their solvents,” *Eur. Phys. J. E*, vol. 39, no. 2, pp. 1–9, 2016, doi: 10.1140/epje/i2016-16012-y.

[67] S. R. Bonney and H. H. Rmaile, “Process of making cold-water dispersible cellulose ethers and uses

thereof," US 20070175361A1, Jan. 2007.

[68] J. Pourchez, P. Grosseau, R. Guyonnet, and B. Ruot, "HEC influence on cement hydration measured by conductometry," *Cem. Concr. Res.*, vol. 36, no. 9, pp. 1777–1780, Sep. 2006, doi: 10.1016/j.cemconres.2006.06.002.

[69] J. Pourchez, A. Peschard, P. Grosseau, R. Guyonnet, B. Guilhot, and F. Vallée, "HPMC and HEMC influence on cement hydration," *Cem. Concr. Res.*, vol. 36, no. 2, pp. 288–294, Feb. 2006, doi: 10.1016/j.cemconres.2005.08.003.

[70] J. Pourchez, P. Grosseau, and B. Ruot, "Current understanding of cellulose ethers impact on the hydration of C3A and C3A-sulphate systems," *Cem. Concr. Res.*, vol. 39, no. 8, pp. 664–669, Aug. 2009, doi: 10.1016/j.cemconres.2009.05.009.

[71] A. M. Betioli, P. J. P. Gleize, D. A. Silva, V. M. John, and R. G. Pileggi, "Effect of HMEC on the consolidation of cement pastes: Isothermal calorimetry versus oscillatory rheometry," *Cem. Concr. Res.*, vol. 39, no. 5, pp. 440–445, May 2009, doi: 10.1016/j.cemconres.2009.02.002.

[72] E. Knapen and D. Van Gemert, "Cement hydration and microstructure formation in the presence of water-soluble polymers," *Cem. Concr. Res.*, vol. 39, no. 1, pp. 6–13, Jan. 2009, doi: 10.1016/j.cemconres.2008.10.003.

[73] Z. H. Ou, B. G. Ma, and S. W. Jian, "Influence of cellulose ethers molecular parameters on hydration kinetics of Portland cement at early ages," *Constr. Build. Mater.*, vol. 33, pp. 78–83, Aug. 2012, doi: 10.1016/j.conbuildmat.2012.01.007.

[74] E. Spychał and P. Czapik, "The Influence of HEMC on Cement and Cement-Lime Composites Setting Processes," *Materials (Basel).*, vol. 13, no. 24, p. 5814, Dec. 2020, doi: 10.3390/ma13245814.

[75] E. Keita, Y. Rifaai, P. Belin, and N. Roussel, "Influence of non-adsorbing polymers on drying of fresh mortars," *Cem. Concr. Res.*, vol. 116, pp. 38–44, Feb. 2019, doi: 10.1016/j.cemconres.2018.10.016.

[76] A. Pierre, D. Weger, A. Perrot, and D. Lowke, "Penetration of cement pastes into sand packings during 3D printing: analytical and experimental study," *Mater. Struct. Constr.*, vol. 51, no. 1, 2018, doi: 10.1617/s11527-018-1148-5.

[77] T. Chevalier *et al.*, "Darcy's law for yield stress fluid flowing through a porous medium," *J. Nonnewton. Fluid Mech.*, vol. 195, pp. 57–66, May 2013, doi: 10.1016/j.jnnfm.2012.12.005.

[78] T. Chevalier and L. Talon, "Generalization of Darcy's law for Bingham fluids in porous media: From flow-field statistics to the flow-rate regimes," *Phys. Rev. E*, vol. 91, no. 2, p. 023011, Feb. 2015, doi: 10.1103/PhysRevE.91.023011.

[79] W. Heber Green and G. A. Ampt, "Studies on Soil Phyics.," *J. Agric. Sci.*, vol. 4, no. 1, pp. 1–24,

May 1911, doi: 10.1017/S0021859600001441.

[80] S. P. Neuman, “Wetting front pressure head in the infiltration model of Green and Ampt,” *Water Resour. Res.*, vol. 12, no. 3, pp. 564–566, Jun. 1976, doi: 10.1029/WR012i003p00564.

[81] G. Ovarlez and N. Roussel, “A Physical Model for the Prediction of Lateral Stress Exerted by Self-Compacting Concrete on Formwork,” *Mater. Struct.*, vol. 39, no. 2, pp. 269–279, Aug. 2007, doi: 10.1617/s11527-005-9052-1.

[82] P.-E. Oren, S. Bakke, and O. J. Arntzen, “Extending Predictive Capabilities to Network Models,” *SPE J.*, vol. 3, no. 04, pp. 324–336, Dec. 1998, doi: 10.2118/52052-PA.

[83] D. Weger and C. Gehlen, “Particle-bed binding by selective paste intrusion—strength and durability of printed fine-grain concrete members,” *Materials (Basel).*, vol. 14, no. 3, pp. 1–18, Jan. 2021, doi: 10.3390/ma14030586.